LATCHING MECHANISM BETWEEN UAV AND UGV TEAM FOR MINE RESCUE

By

Sarah Hoffman, B.S.

A Project Submitted in Partial Fulfillment of the Requirements

for the Degree of

Master of Science

in

Mechanical Engineering

University of Alaska Fairbanks

August 2017

APPROVED:

Rorik Peterson, Committee Chair
Michael Hatfield, Committee Member
Chuen-Sen Lin, Committee Member
Rorik Peterson, Chair
Department of Mechanical Engineering

Abstract

Safety is a concern in the mining industry when a tunnel collapse could result in the casualties and deaths of workers and rescuers due to the hazards posed to them. The Alaska Center for Unmanned Aircraft Systems Integration (ACUASI) is working on a project to increase mine safety by sending an Unmanned Ground Vehicle (UGV) fit with LiDAR sensors and an Unmanned Aircraft Vehicle (UAV) to map the tunnels and to find a collapsed tunnel in an effort to determine the location and condition of trapped workers. The UGV will drive to the collapsed tunnel, at which point the UAV will launch to find any gap in the tunnel that it could fly through to assess the damage. This overall project requires a releasing and latching system to secure the UAV, allow it to launch at the appropriate location, and dock the UAV when its mission is complete or its battery needs recharging. A simple pin-through design was adopted to latch and release the UAV by implementing a Scotch yoke and servo as the actuator. All necessary components were analyzed for stress using two forces, 16 N (maximum takeoff weight of the potential UAV) and 150 N (impact force of the maximum weight of the potential UAV from 0.15 m or just under 6 inches). Three sets of properties for PLA were applied in the stress analyses to thoroughly investigate the feasibility of creating the parts out of PLA, a commonly used plastic for 3D printing. These three property sets were found in literature and consisted of bulk values of PLA, empirically determined values of 3D printed PLA, and values calculated using porosity equations. It was found that most components would function satisfactorily without risking fracture except in extreme conditions. The stress analyses for the landing gear illustrated its weaknesses, revealing a potential need for a different material or redesign. The landing gear as it is could be utilized under nominal operation, but it could not withstand any significant impact such as one that might occur in the event of a hard landing. The latching mechanism itself succeeded in securing the UAV. Future work includes redesigning the landing gear, another design concept for a latching mechanism that may prove more reliable, and adjusting the landing pad in the event a different UAV is selected.

Table of Contents

List of Figures

Page

List of Tables

Page

Acknowledgements

I would like to thank my committee for their patience and understanding, Dr Rorik Peterson for his support and advice as the committee chair, Dr Michael Hatfield for keeping me on track and advocating on my behalf so that I could get paid through ACUASI for working on this project, and Dr Chuen-Sen Lin for his advice and expertise with the simulations of SolidWorks. My project was supported in part by the Mechanical Engineering Teaching Assistantship, the Geophysical Institute Research Assistantship, and the Alaska Center for Unmanned Aircraft Systems Integration. Many of the assets purchased and supporting work done by ACUASI were made possible by Mine Safety and Health Administration (MSHA).

I would also like to thank Sam Vanderwaal for his electrical engineering wizardry and Isaac Thompson and Sam Jeffries for their suggestions and assistance.

Chapter 1. Introduction

1.1. Background

1.1.1. Mine Safety

Since the beginning of mining history, safety has been a prime concern, most notably in regards to subsurface mining. There are many dangers involved in the event of a tunnel collapse, both to any unfortunate workers trapped within the mines, as well as to those attempting to extricate them. Hazardous gases and the potential continuation of collapse pose immense risks to any human rescue team. According to the National Institute for Occupational Safety and Health (NIOSH) under the Centers for Disease Control and Prevention (CDC) [1], there were 26 mining occupational fatalities reported in 2015 in the United States, 11 of these occurring at underground work locations, and the fatality rate is much higher for underground workers than for surface workers (20.8 versus 7.0 per 100,000 full time equivalent workers). The causes of fatalities are broken down into five categories for the total 26 fatalities: Machinery at 30.8%; Powered haulage at 23.1%; Fall of ground at 15.4%; Falling, rolling, or sliding rock or material at 15.4%; and All other at 15.4% [1]. Additionally, there were 4,517 nonfatal lost-time injuries in 2015; 1,503 (or 33.3%) of these occurred underground [1]. Comparing this data to that from 2014 could possibly indicate improvements in safety as there were less fatalities and injuries in 2015; however, these numbers can still decrease. The Mine Safety and Health Administration (MSHA) [2] discusses the process for a rescue operation, and the biggest influence on the length of time it takes during such an operation is the necessary concern of the safety of the rescuers, specifically with regards to their ability to breathe as a fresh air base must be set up and gradually expanded. A robot, however, does not need to breathe.

To ameliorate the situation, unmanned vehicles can be utilized in the initial stages of a rescue mission to detect the location of those trapped within; potentially provide immediate assistance before human rescuers are able to arrive, mitigating the risks posed to human life; and maximize the efficacy of a rescue team's capabilities by providing actionable data before and after rescuers enter the mine when these vehicles are aptly equipped to help save lives. An unmanned ground vehicle (UGV) can navigate a mine's tunnels while outfitted with numerous sensors

including Light Detection and Ranging (LiDAR) technology which can be used to create a map of the tunnels and avoid collisions with the walls and any other obstacles. Adding an unmanned aerial vehicle (UAV) to the UGV's payload augments the system's capabilities by allowing additional coverage when the ground vehicle reaches a point at which progression is impeded by land-based obstructions such as resultant debris from a tunnel collapse. The UAV, also equipped with LiDAR and associated sensors, can then be released from the UGV and resume the search for stranded workers. The Alaska Center for Unmanned Aircraft Systems Integration (ACUASI) is working toward this overall goal by connecting UAF students of varying technical backgrounds to different facets of the project as a whole.

This project requires a releasing and latching system to secure the UAV, allow it to launch at the appropriate location, and dock the UAV when its mission is complete or its battery needs recharging. This paper investigates various docking and latching mechanisms suitable for the underground mining environment that will make it possible for the UAV to dock with the UGV. The components of the latching mechanism are analyzed and optimized for strength, weight, and feasibility while utilizing a suitably simplistic design for an extreme environment.

1.1.2. Solid Mechanics

Solid mechanics, also referred to as mechanics of materials, is the study of solid materials undergoing deformation, typically but not exclusively as a result of applied forces [3]. A body's strength and rigidity can be represented by its stress and strain, respectively. The simple definition of stress is a force over an area, and strain is defined as total deformation over total characteristic length. One can plot stress of an object versus its strain to attain a curve characteristic of the material's properties, independent of the object's dimensions. The beginning of this curve is known as the elastic region, in which the stress and strain are directly proportional and the material can return to its initial shape should the load be removed. Known as Hooke's Law, this can be written as

$$\sigma = E\epsilon \tag{1.1}$$

where σ is the stress and ϵ is the strain. The coefficient E is a material property called the modulus of elasticity or Young's modulus.

The stress at which a material ceases to undergo elastic deformation and instead is subjected to plastic deformation can be approximated as the material's yield strength, whereupon Hooke's law no longer applies and the material retains strain after the load is removed. The yield strength can be determined by drawing a line parallel to the initial linear slope with an offset of 0.002 strain (designated as 0.2% offset); the point at which this parallel offset intersects with the stress-strain curve is defined as the yield strength by this method [4]. This is illustrated in Figure 1.1 below; the yield strength is denoted by σ_Y and the point Y indicates the estimated yield point by the 0.2% offset method. The maximum stress a material can withstand is known as its ultimate strength, which is also referred to as the Ultimate Tensile Strength (UTS) when the material is in tension. This is an important material property to consider in design due to the fact that once an object reaches its ultimate strength it is likely to break shortly thereafter.

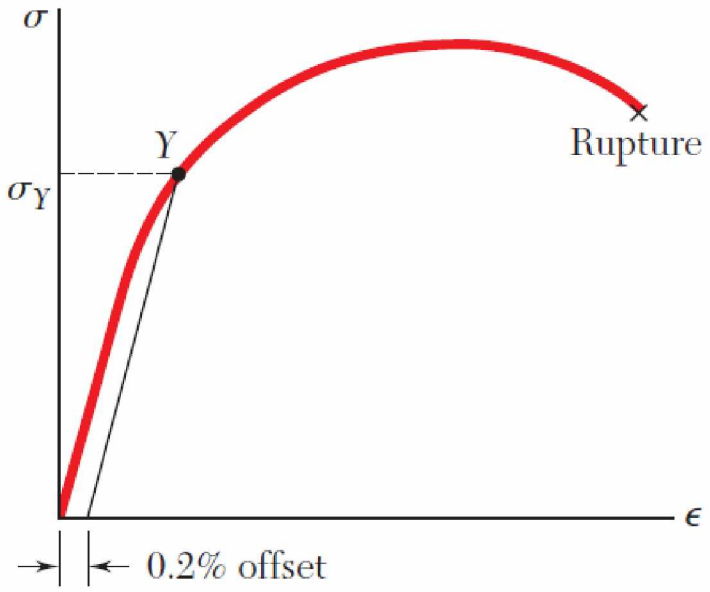

Figure 1.1: Determination of yield strength by offset method [4]

When designing a part in the 3D Computer Aided Design (CAD) software SolidWorks, one can analyze the part's stress and strain given a material's properties using finite element analysis. The program's linear stress analysis utilizes Hooke's Law and thus assumes that the part is subjected to only elastic deformation [5]. If the maximum stress achieved in this method is less than or equal to the yield strength, the results can be considered valid; however, if the maximum

stress is higher than the yield strength, it may be prudent to either redesign or select a different material regardless. Additionally, SolidWorks provides a nonlinear alternative for the instances when the yield stress is exceeded for more accurate solutions [6].

In order to fully understand the analyses produced from the SolidWorks simulations, a few more concepts must be known. Many failure criteria rely on the use of principal stresses. Boresi and Schmidt [7] write:

> "For any general state of stress at any point 0 in a body, there exist three mutually perpendicular planes at point 0 on which the shear stresses vanish. The remaining normal stress components on these three planes are called principal stresses. Correspondingly, the three planes are called principal planes, and the three mutually perpendicular axes that are normal to the three planes (hence, that coincide with the three principal stress directions) are called principal axes. Thus, by definition, principal stresses are directed along principal axes that are perpendicular to the principal planes. A cubic element subjected to principal stresses is easily visualized, since the forces on the surface of the cube are normal to the faces of the cube."

The process for determining these principal stresses is straightforward but superfluous for this paper to explicate. Beer et al. [4] present the fundamentals effectively.

There are two main criteria for ductile materials assessing failure of a design, the maximum shearing stress criterion (or Tresca criterion) and the maximum distortion energy criterion (or von Mises criterion) [4, 7]. The Tresca criterion observes that the slippage of a ductile material along oblique surfaces causes yield predominantly through shear stress, and under this criterion, a component is considered safe so long as the maximum shear stress does not exceed the stress that results in yield during a tension test [4]. The maximum shear stress is determined using Eq (1.2), where σ_1, σ_2, and σ_3 are principal stresses and τ_1, τ_2, and τ_3 are shear stresses [7].

$$\tau_1 = \frac{|\sigma_2 - \sigma_3|}{2} \tag{1.2a}$$

$$\tau_2 = \frac{|\sigma_3 - \sigma_1|}{2} \tag{1.2b}$$

$$\tau_3 = \frac{|\sigma_1 - \sigma_2|}{2} \tag{1.2c}$$

The maximum shear stress, τ_{max}, is the largest result of these three equations; if τ_{max} is greater than or equal to half of the yield strength, the Tresca criterion is met and predicts failure for the component [7].

Under the von Mises criterion, yielding occurs when the energy associated with changes in shape (distortion energy) at a point equals the distortion energy at yield in a tension test [4, 7]. The von Mises stress, $\sigma_{vonMises}$, can be written in terms of the principal stresses, as shown in Eq (1.3) below [7].

$$\sigma_{vonMises} = \sqrt{\frac{1}{2}[(\sigma_1 - \sigma_2)^2 + (\sigma_2 - \sigma_3)^2 + (\sigma_3 - \sigma_1)^2]} \tag{1.3}$$

Predicted failure ensues when $\sigma_{vonMises}$ is greater than or equal to the yield strength [4, 7]. For the case of torsion, the maximum shear stress can be calculated using Eq (1.2), and the von Mises criterion can be expressed as Eq (1.4) where τ_y is the shear yield stress and σ_Y is the tensile yield strength [4, 7].

$$\tau_y = \frac{\sigma_y}{\sqrt{3}} \tag{1.4}$$

This allows an easy comparison between the Tresca and von Mises criteria; the Tresca criterion predicts failure when the maximum shear stress reaches $0.5 \cdot \sigma_Y$ while the von Mises criterion predicts failure when the maximum shear stress reaches $\sigma_Y/\sqrt{3}$ or $0.577 \cdot \sigma_Y$. From this comparison, it can be seen that the Tresca criterion provides an extra amount of safety in determining yield and is considered to be more conservative in its estimations. Beer et al. [4] provides a graphical representation of this shown in Figure 1.2 below. Due to notation differences between [4] and [7], σ_a and σ_b here represent two principal stresses. The hexagon is the result of the Tresca criterion, and the ellipse is from the von Mises. While the Tresca criterion is considered more conservative, the von Mises criterion is considered to be more accurate, at least in regards to predicting yield under pure shear [4, 7].

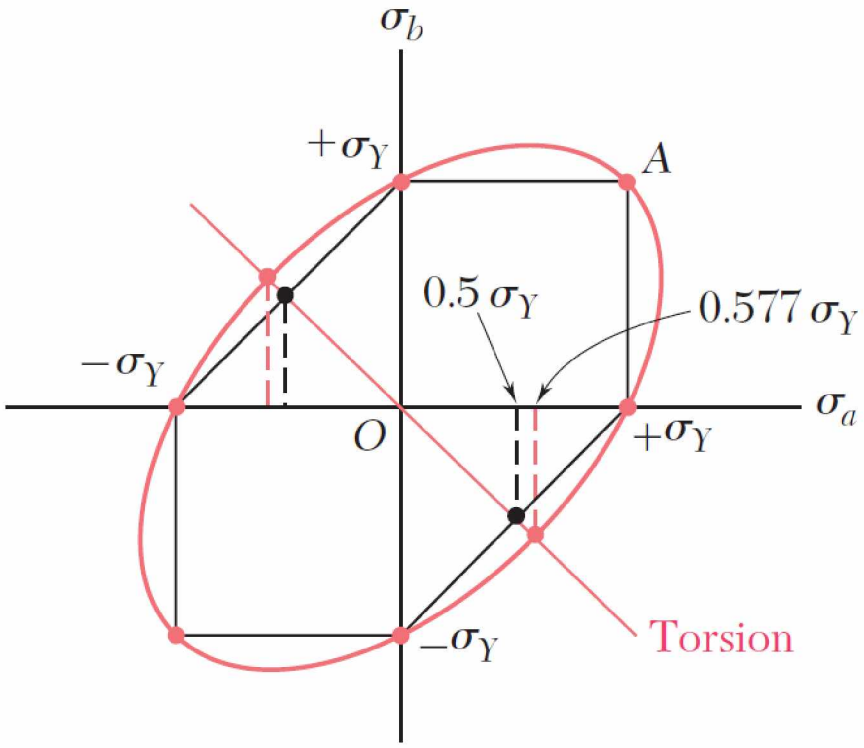

Figure 1.2: Graphical comparison of Tresca and von Mises criteria [4]

SolidWorks provides both of these methods, but the software calculates and best represents the stresses as von Mises stresses. In Chapter 3, stress analyses will be given for various components. The von Mises criterion was selected for failure predictions to avoid confusion over the method of calculating the stresses and the method of determining failure. Assumptions were made to build in an additional level of safety to compensate for the less conservative predictions generated through the von Mises criterion.

1.1.3. Additive Manufacturing

Additive manufacturing with 3D printers can be used to make prototypes, and in many cases final products, very quickly and relatively inexpensively with less effort than machining. This technology allows for the production of complex and odd architectures, as well. This capability proves to be invaluable in creating structural support for mounting systems in a suitable configuration. The dimensions and feasibility of a part can be physically examined within a few hours, and the final part can be similarly fabricated, depending on its requirements. Many different

materials can be used for 3D printing, most commonly the plastics PLA (PolyLactic Acid) or ABS (Acrylonitrile Butadiene Styrene); if the part is integral to the system and undergoes significant stress so that the potential stability is in question, the part can be replaced and fabricated from a stronger material such as a more robust plastic or even some metals like steel and aluminum. Since PLA is the easiest material with which to print, it has been selected for all initial 3D printed parts for this project.

Fused deposition modeling (FDM) is the type of additive manufacturing most frequently seen in today's 3D printers and facilitates fabrication by implementing a hot end or extruder to melt material pushed through a nozzle and a set of stepper motors to then move the nozzle in a programmed pattern, dragging the melted filament across a flat surface that can travel vertically. Because of this process, components thus manufactured exhibit anisotropy, and so the mechanical properties are dependent on direction. One of the most important factors in a component's strength, therefore, is print orientation [8-15]. Figure 1.3 below from Lee et al. [10] illustrates what is meant by print or build orientation. A component should be printed such that the build direction runs perpendicular to the estimated applied force vector so that the filaments of each layer will run parallel.

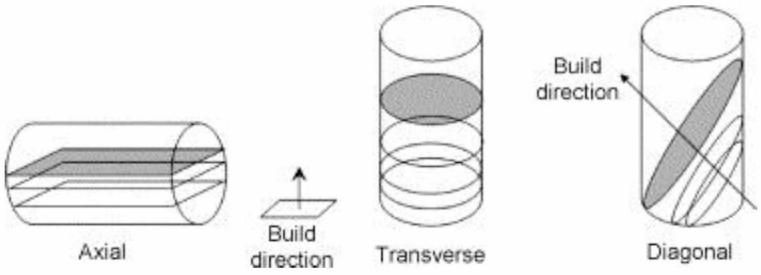

Figure 1.3: Definition of build direction [10]

Other factors contribute to the mechanical properties of 3D printed parts to a lesser extent, such as the layer thickness [9, 10, 12-16] and the infill [11, 12, 14, 16, 17]. Parts can also undergo treatment, such as heat treatment [16] or, specifically for ABS, extended exposure to acetone vapor [18], smoothing the layers together to increase the strength.

Due to the anisotropic quality of 3D printed parts, the mechanical properties of the bulk material cannot be used to accurately describe the parts' strength but can act as an upper bound. Lanzotti et al. [13] proffer values for the UTS and Young's modulus specifically for 3D printed

PLA, which will be used as a midrange estimation as these values agree with those of Tymrak et al. [15]. Choren et al. [19] summarize research into the effects of porosity on materials and include equations to calculate the Young's modulus and tensile strength when given a bulk value of a material and the porosity of the component. Although these equations do not include enough information to confidently compute mechanical properties of 3D printed parts and only consider porosity without build orientation, they can function as a lower bound estimation.

For the ultimate tensile strength, Choren et al. [19] provide only two equations, which Knudsen [20] writes are approximately the same if the proportion between the empirical constants is slightly altered. The equation with more data available was selected and is given by Eq (1.5) where S_P is the UTS of the porous body, S_0 is the UTS of the bulk material, k is a constant dependent on the material, and P is the volume porosity.

$$S_P = S_0 exp(-kP) \tag{1.5}$$

Knudsen [20] writes that the values of k "ranges from 6 for the 'most porous' cubic arrangement to 9 for the 'least porous' rhombohedral arrangement." The value of k used in this project's calculations was 8.

In regards to the Young's modulus, Choren et al. [19] present numerous equations and the assumptions about the material's porosity and pore shape that determine which equation should be used for a given composition. Similar to the previous selection, Eq (1.6) was chosen, where E_P is the elastic modulus of the porous body, E_0 is the elastic modulus of the bulk material, and y is a constant calculated by Eq (1.7) using the bulk material's Poisson's ratio, υ_0.

$$E_P = E_0 \frac{(1-P)^2}{1+yP} \tag{1.6}$$

$$y = 2 - 3\upsilon_0 \tag{1.7}$$

If the porosity is greater than 0.4 for Eq (1.6) or 0.5 for Eq (1.5), the equations will not produce valid results, and so further measures must be made to ensure the porosity remains below 0.4 [19]. Choren et al. [19] do not mention how the volume porosity might be calculated when considering a 3D printed component, however; this will be explored further in Chapter 3.

1.2. Literature Review

The concept of using unmanned vehicles in dangerous situations to minimize risk to human life is not novel, and in fact, UGVs have been utilized for various purposes such as bomb disposal [21], volcanic observation [22], mine detection and disposal [23], and have even been considered for the exact objective of this overall project: mine rescue [24]. UGVs and UAVs have been used together as teams for both mapping [25] and human detection and localization [26], two aspects of the overall project. However, most operations for both UGVs and UAVs are outdoors and can depend on GPS, whereas a mine presents a dark, GPS-denied environment. Some further considerations must be made for such a scenario.

In order to map the tunnels of a mine, avoid obstacles, and detect a collapse, the UGV can make use of algorithms for SLAM [27, 28] or Simultaneous Localization and Mapping, sometimes referred to as CML, Concurrent Mapping and Localization. Dhiman et al. [27] write, "Planning to move to a specific location involves the following three activities: (i) path planning, (ii) localization, and (iii) mapping." Localization involves estimating the UGV's position and orientation relative to a map, and mapping involves creating a spatial model of the surroundings [27]. This can be carried out utilizing LiDAR sensors, which can also be used on the UAV for similar purposes as with the UGV (namely mapping, obstacle avoidance, and detection of a collapse or gap) and additionally as an aid for automated landing [28-31].

Many automated landing techniques still require visual data as a method of localizing the UAV [26, 28, 31-33]. In the dark environment of a mine, this can be managed using lights mounted on the UAV to act as references for a sensor to identify the positioning of the UAV with respect to the UGV. Once the UAV has landed, it will need to recharge its battery to continue the mission due to the UAV's limited flight time; this can be performed by a contact similar to the pin-in-flexible-louver system found in [34] or through inductive charging, which is significantly less efficient and therefore takes longer to charge [34]. The battery could also be swapped out with a fully charged set, as in [35, 36], for a potentially quicker method.

While an automated landing system may be fairly precise, it is highly improbable that it will be exact. To ease the tolerances of the landing system, a passive guiding system may be implemented to bring the UAV's landing gear into position for docking, as was the case for [34, 37, 38], or a system of positioning levers that actuate independently may be used to move the UAV

into the docking position, as was the case for [39]. Once the UAV has reached its docking position at the end of the funnel, the latching mechanism can engage.

The latching mechanism's sole purpose is to firmly hold the UAV in the docking position during transit and recharging. This can be accomplished through electromagnets if a piece of ferromagnetic material is attached to the UAV, as was used in [34]. Electromagnets draw too much power for this to be a constant method for securing the UAV but could be used temporarily to grasp the UAV and hold it in place while a primary latching mechanism activates or if a particularly big bump is detected ahead. Including electromagnets in the system also allows a secondary source of securing the UAV remotely should the primary mechanism fail.

As for the primary latching mechanism itself, there are few examples of such a problem in literature. A system similar to the probe and drogue approach of air-to-air refueling [40] could be used in which the "drogue" portion with controlled surfaces, although not utilized for aerodynamic purposes, could act as the funneling system and the "probe" could be the ends of the landing gear and contain contacts for recharging the battery. Another potential source of inspiration could be the mechanism used for On-Orbit Servicing, stations for servicing satellites; these stations use clamps to grasp the satellite [41]. A new method for grasping spacecraft on-orbit was proposed in [42] which uses a pantograph that contracts once the spacecraft is docked to hold both the servicing and serviced spacecrafts together. Below, Figure 1.4 from [42] depicts this. On-Orbit Servicing designs for latching or grasping mechanisms are necessarily focused on the more complicated scenario of low gravity, however, and so such a robust system may be considered exorbitant.

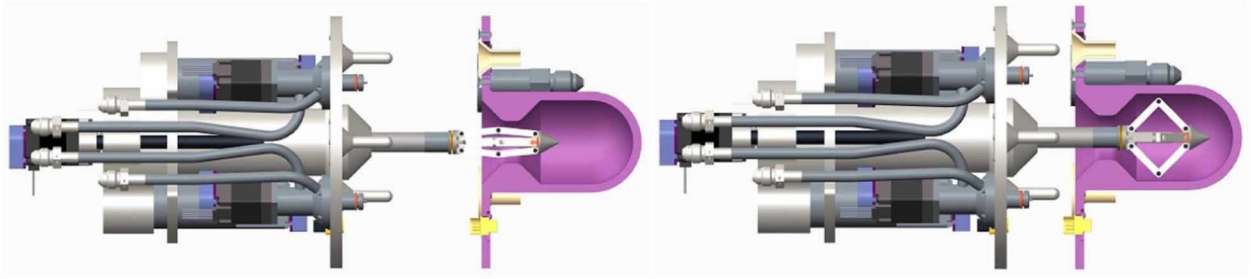

Figure 1.4: Pantograph getting introduced into the drogue cavity; initial entrance (left) and deployment (right) [42]

Byun et al. [38] investigated a conceptual design of a UAV/UGV team with a spherical UAV and a concave docking interface on the UGV. The interface proposed has locking devices that both handle the UAV after it lands to position it in the required orientation to recharge and also hold the UAV to the UGV. To illustrate this, Figure 1.5 from [38] is shown below.

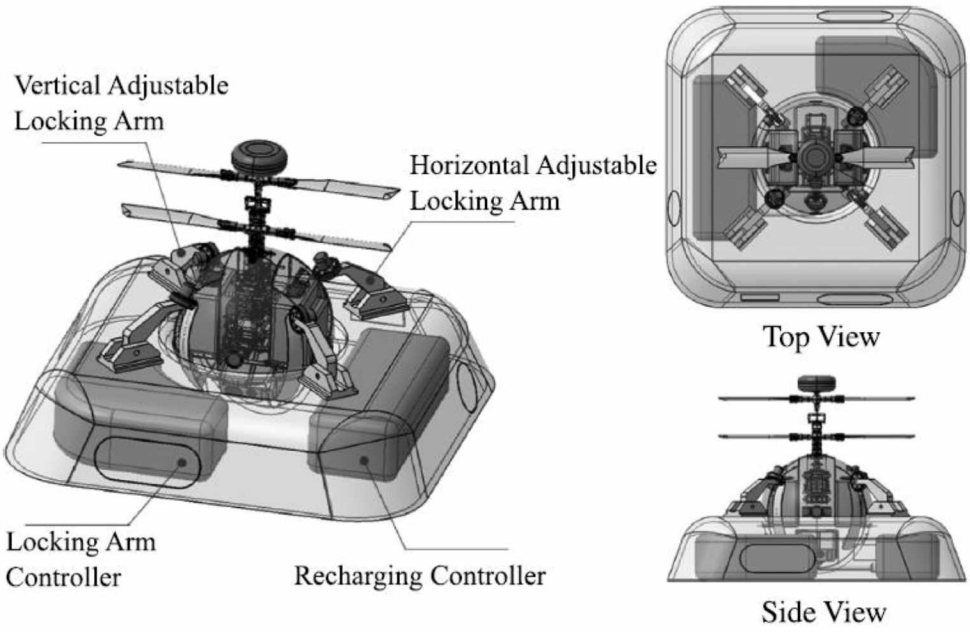

Figure 1.5: Comprehensive schematic design result of the docking interface [38]

From this literature review, a few points in consideration of designing a latching mechanism for securing a UAV to a UGV have become apparent: 1) a guiding system, whether passive or active, should be present to ensure the landing UAV reaches the appropriate docking position; 2) there exists several methods of securing two vehicles together; and 3) while the previous statement is true, there exists only a few examples in literature of investigation into this specific problem.

1.3. Scope

It is ACUASI's goal to create a UGV/UAV team for the purposes of mapping out mine tunnels and locating trapped miners. The scope of this project is to support ACUASI's effort to increase mine safety by creating a latching system to secure the UAV to the UGV for transport. This latching mechanism must be capable of remotely or programmed releasing its hold on the

UAV so that the UAV can launch from the deck of the UGV and latching once again upon the UAV's docking. The UAV must be held firmly in place during transport and must allow for recharging of the UAV by the UGV's battery.

Chapter 2. Design

2.1. Design Considerations

In order to allow more tolerance in the landing system's accuracy and as seen in the literature review, a guidance system, either active or passive, will need to be included in the docking system. A passive guidance system would not require power and so would be better suited for this project's purposes. This guidance system, or funneling array, should be attached to the UGV's deck in such a way that the UAV is under vibration damping and that the UAV's landing gear does not collide with the side of the funneling array on approach, resulting in the UAV tipping as it attempts to land and in a potential impact of the UAV's propellers. This requires the funneling array to be mounted under or flush with the UGV's top deck. This combined with the dimensional load of the UAV necessitates a new or supplemental plate design for the UGV. Vibration damping balls typically used for camera gimbals offer sufficient damping for the purposes of this project and operate most effectively in compression, and so a fixture must be devised to accommodate the below-deck suspension of the funneling array to attach the damping balls such that they will react in compression to a load applied to the array.

While landing gear is available from the manufacturer of the UAV, a customized set is desired to allow for the securing method to incorporate the landing gear in its conception; additionally, the UAV will need to recharge its batteries from the UGV to conserve time and energy in the rescue operation, and so it is necessary for the landing gear to include the recharging system in its design. The latching mechanism should be designed with a relatively low power consumption in consideration to eschew overburdening the UGV's battery. Furthermore, the latching mechanism must be capable of remotely securing and releasing the UAV.

There are other considerations in the enveloping task that must be examined, such as for the automated landing, obstacle avoidance of both vehicles, and communications. However, these considerations lie outside of the scope of this project and as such only brief coverage in the literature review will be provided to give perspective on the main objective and how everything is connected. The subsequent materials are thus only for the latching mechanism and do not include necessary sensors or equipment for the operation of the assorted systems.

2.2. Materials

2.2.1. Unmanned Ground Vehicle

It is imperative that the ground vehicle be able to transport and power the sensors in the endeavor to locate the mine collapse. The UGV must be able to carry its battery, the sensors, the landing pad, and the UAV with its sensors and battery. Since the UGV's battery will also be used to recharge the UAV, an extra battery set may also need to be hauled into the mine.

The Husky from Clearpath Robotics, also used in [43] and pictured in Figure 2.1 below, was chosen as the UGV. It has a carrying capacity of 165 pounds (75 kilograms) and a maximum speed at 2.3 miles per hour (1.0 meters per second) with a run time of 3 hours in typical use. The maximum angle that it can climb is 45 degrees and that it can traverse is 30 degrees [44]. While the deck of the Husky would be voluminous enough to land a UAV, it must also carry various sensors in addition to spare batteries, and thus a landing pad is also required.

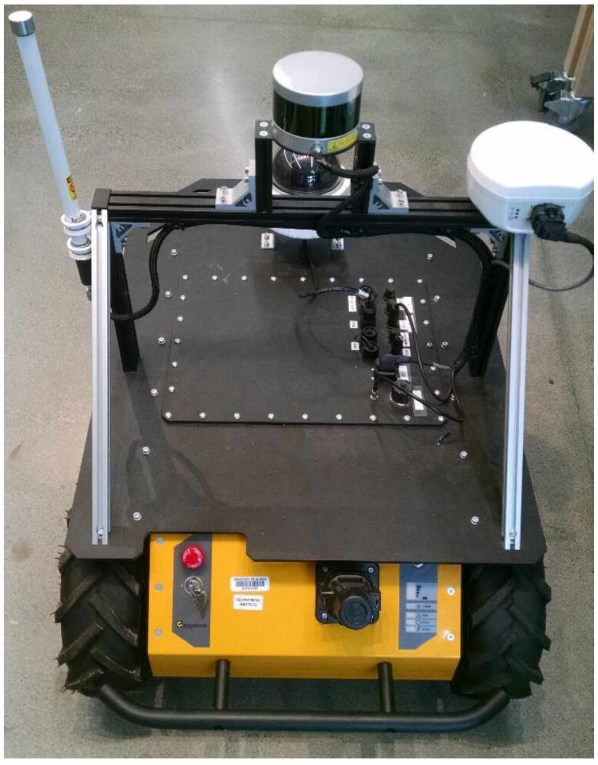

Figure 2.1: Unmanned ground vehicle Husky from Clearpath Robotics

2.2.2. Landing Pad

Due to the dimensional load of the UAV, a larger deck or an extension of the existing Husky plate must be constructed to include a platform from and on which the UAV will launch and land. The funneling array must also be flush with the plate, as mentioned previously, and so the landing pad needs to accommodate this. Figure 2.2 depicts the landing pad that was designed by graduate student Isaac Thompson based upon design specifications provided by the author and created out of aluminum. The landing pad has cut-outs where the funnels are to be placed; this configuration is for a specific UAV footprint.

Figure 2.2: Aluminum landing pad extension created by Isaac Thompson

2.2.3. Unmanned Aerial Vehicle

The unmanned aircraft vehicle adds a dimension to an unmanned search and rescue team in that vertical distance can also be covered to allow for a new perspective. The UAV must be able to carry many sensors and fly for a significant amount of time. The UAV should also be replaceable as it is entering a hazardous environment from which it may very likely not return, and so it should be relatively inexpensive.

The UAV chosen for concept of operations and designing stages was the Flame Wheel F450 by DJI, which has a maximum takeoff weight listed as 1600 grams [45]. Figure 2.3 below depicts the F450 in testing configuration. As this UAV was also used in [46] for autonomous landing on an unmanned boat, it likely suites this project's needs.

Figure 2.3: DJI's F450 in a testing configuration

2.2.4. Actuator

Regardless of the design, a mechanism that latches and releases will require parts that move. This means an actuator of some sort must be present to receive and implement commands. An easy to obtain and command actuator is a servo or motor, and so a servo was selected among those that were at hand for the development and design of a latching mechanism. This servo, the Hitec HS-322HD, is shown below in Figure 2.4.

Figure 2.4: Hitec servo HS-322HD

2.2.5. Securing Mechanism

The securing mechanism is the primary ingredient to this project, and its design will be discussed in the subsequent chapters. The latching mechanism is what will directly connect to the UAV and physically restrain it to resist motion induced by the UGV's movement. Its design must take into consideration a low power draw and durability as well as an acceptable failure state.

2.3. Design Strategy

The latching mechanism was designed using SolidWorks and the analyses it provides. The two main parts that aid in securing the UAV are the landing gear and the countersunk funneling array as these provide a holding point between the UAV and UGV respectively, and so their design, analyses, and implementation will be discussed. A simple approach to securing the UAV was used first with other methods developed for further investigation. The development of the latching system is described in the following chapter.

Chapter 3. Development

3.1. Analysis

SolidWorks provides methods for analyzing the stresses of a component so long as necessary information about the component's material is provided. This is a simple matter for well-known, homogeneous materials such as steel or aluminum alloys, but when considering 3D printed components, additional thought must be put into the properties before calculating the stress. As previously discussed in Chapter 1, three considerations for the material properties of PLA will be used for analyzing the stresses of each component: 1) the bulk values provided by [16], 2) 3D printed PLA values provided by [13] with a yield strength calculated from the results of [16], and 3) values calculated using equations dependent on porosity provided by [19]. As [19] does not include calculations for yield strength, the UTS will be inputted in SolidWorks as both the yield and tensile strengths; if this value is nearly reached, the part may undergo plastic deformation.

Choren et al. [19] provide equations to calculate the Young's modulus and UTS dependent on the porosity of the material but do not mention how the volume porosity might be calculated when considering a 3D printed component. Therefore, a logical method must be developed to give a reasonable estimation. The definition of volume porosity used in [19] is assumed to be the volume of void spaces or pores divided by the total volume. Among the various data SolidWorks grants the user from a given part file, the part's surface area and volume can be determined. However, a 3D printed component can have various percentages of infill and shell thickness that come into play when determining the porosity and does not have a homogeneous porosity. A sketch of a 3D printed part's cross-section is depicted below in Figure 3.1.

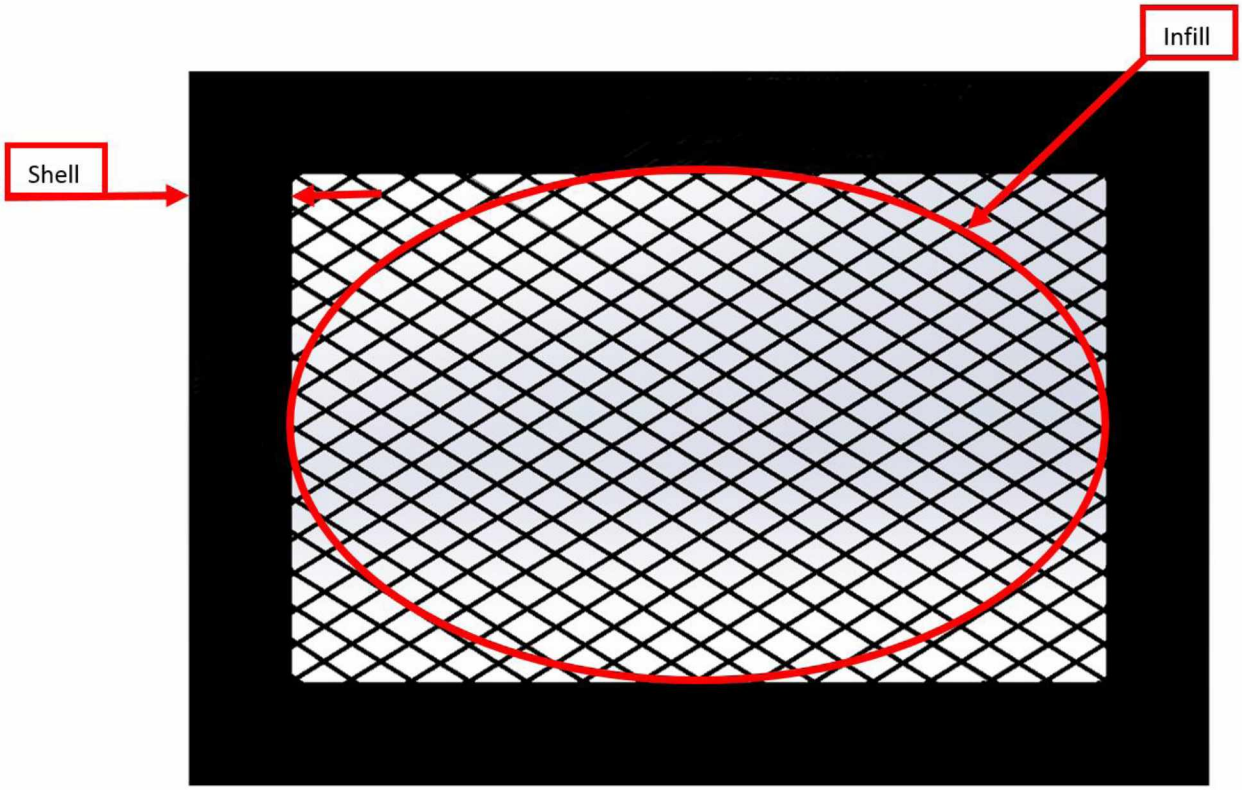

Figure 3.1: Sketch example of a 3D printed part's cross-section

Given a set infill percentage and shell thickness with a component's surface area and total volume, the component's porosity can be estimated by the following method:

1. Multiply the shell thickness (set to 1 mm) with the part's surface area. This is the shell volume.
2. Subtract the shell volume from the total volume. This is the volume that will be occupied by infill and pores.
3. Multiply the infill percentage (set to 35% or 0.35) by the volume obtained in step 2. This is the infill volume.
4. Add the shell volume with the infill volume.
5. Divide the result of step 4 by the total volume. This would give the percentage of solid if multiplied by 100%.
6. Calculate 1 - (result from step 5). This gives the porosity.

If the porosity is greater than 0.4 for Eq (1.6) or 0.5 for Eq (1.5), the equations will not produce valid results [19], and so a sufficient infill percentage has been selected to ensure the porosity remains below 0.4. Since this method is dependent on the part's surface area and volume, this

calculation must be repeated for every part. As noted earlier, this can only provide an estimation due to the nonuniform nature of 3D printed components. The porosity-based PLA material properties provide a minimum estimation of strength and do not take into account that a 3D printed part has a mostly nonporous solid shell supported by the porous infill on the inside. The final results using the equations from [19] are extremely low in comparison to the bulk values of PLA given in [16] and to the 3D printed values given in [13], and so any part that does not exceed a calculated UTS from [19] in a given scenario is highly unlikely to break. If a stress analysis reveals that a part would exceed the calculated UTS from [19], however, that part may not break if the values from [13] and [16] are not exceeded. If the part would exceed the UTS from the bulk PLA value from [16], the 3D printed component will probably result in failure. The material properties of bulk PLA [16] and 3D printed PLA [13, 16] are given in Table 3.1 below.

Table 3.1: Material Properties of Bulk and 3D Printed PLA

Material Property	Bulk PLA Value from [16]	3D Printed PLA Value from [13]
Elastic Modulus (E), MPa	3500	3326.77
Poisson's ratio (υ)	0.36	--
Yield Strength (σ_Y), MPa	70	34.66 [16]
UTS, MPa	73	52.3

For each stress analysis, a force of 16 N was used since the maximum takeoff weight of the UAV is 1600 g or 15.70 N. While ideally no single component should receive the full weight of the aircraft which should be distributed, an additional level of safety can be built into the stress analyses if the full weight is utilized. However, if the UAV were to drop, the impact force of this would be much higher. This force is also used for stress analyses and is estimated using Eq (3.1) from [47] as follows, where m is the mass of the object, g is the gravitational acceleration, h is the height at which the object falls, and s is the distance the object deforms to slow down.

$$F = {}^{m \cdot g \cdot h}/_{s} \tag{3.1}$$

Using the mass of 1600 g, a height of 0.15 m (or a fall of about 6 inches), and a slowdown distance of 0.016 m (dependent on the flexibility of the material and part), this force is calculated

as around 150 N. If a part is shown to fracture under this impact, a different material may be required.

In most of the stress analyses, the maximum stress for each of the three sets of material properties were the same, but due to the differences in UTS values, this maximum stress may exceed one but not the other two. Therefore, only the most significant instance at which the component fails will be shown in most cases. Namely, if the part exceeds the yield strength with bulk PLA as the material at 16 N force, it will exceed the yield strength in all other analyses, and so it would be redundant to include more than the first plot.

To better understand and visualize why the forces are being applied in the manner they are in the following analyses, Figure 3.2 below shows a sketch of the UAV landing on the platform.

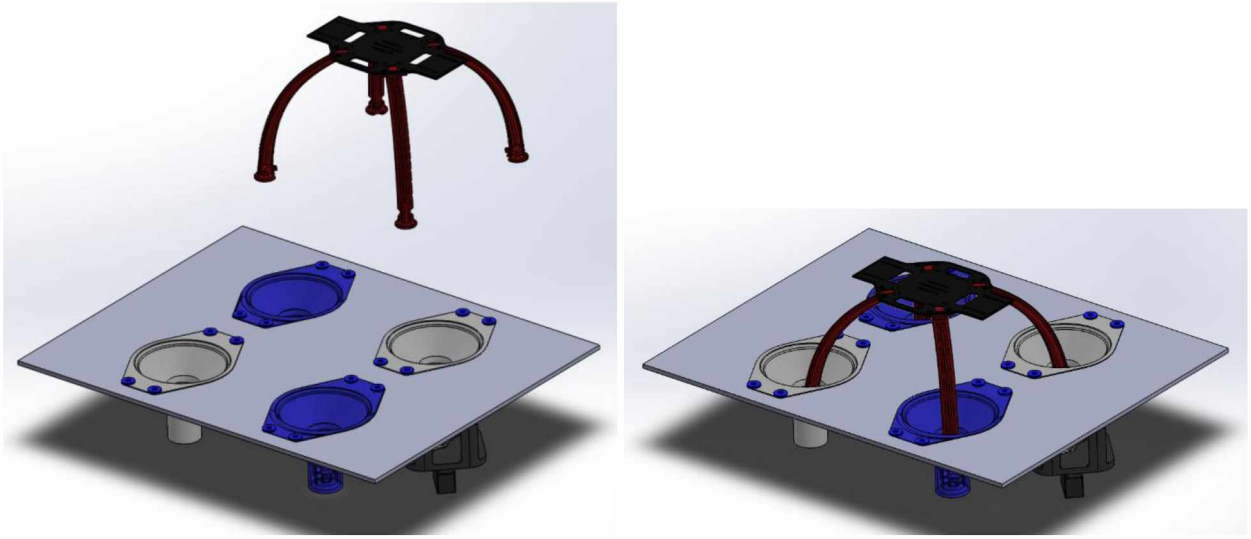

Figure 3.2: Sketch of UAV landing for aid in visualizing forces

3.2. Landing Gear

The UAV from DJI has landing gear from the manufacturer. However, a new design for the landing gear allows it to be incorporated into the design of the latching mechanism, and so the first step for the development of the latching mechanism was to design a new leg for the F450. This leg went through multiple iterations as the design for the latching mechanism became more defined and as the limitations of 3D printed parts were demonstrated in the real world. Figure 3.3 below shows most of these iterations, starting with the default landing gear on the far left and ending with something close to the final design on the far right.

Figure 3.3: Landing gear design progression from left (manufacturer) to right

The first landing gear designed was meant to mimic the manufacturer's landing gear while maintaining strength as it would be of a different material and to demonstrate the latching mechanism concept of a simple "pin-through" design. Clips for the wires that led up to the UAV's batteries were added but later removed when they proved insufficient at holding the cables and zip ties were required. A few hard landings resulted in failure of these legs, as can be seen in Figure 3.4.

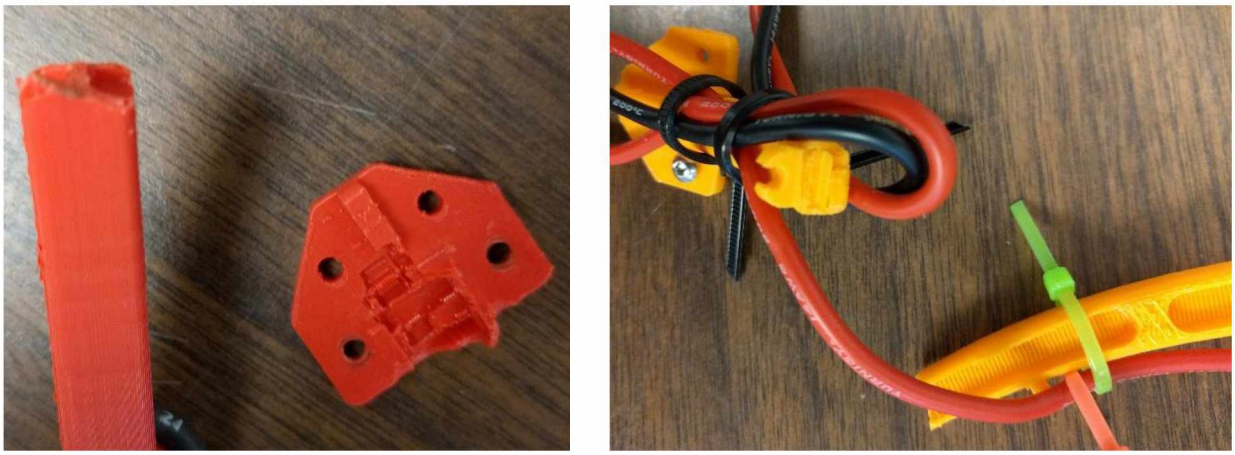

(a) (b)

Figure 3.4: Landing gear failures as a result of hard landings

The conditions occurring during these failures can be compared to the stress analyses to see how well it predicts the rupture of a part. The stress analysis for the original landing gear custom design with a force of 150 N applied to the bottom with the top fixed and the Bulk PLA as a material can be seen below in Figure 3.5. The short, green arrows on the top portion show that face is fixed while the longer, purple arrows on the bottom portion represent force vectors. This notation is standard across all the stress analyses included in this report.

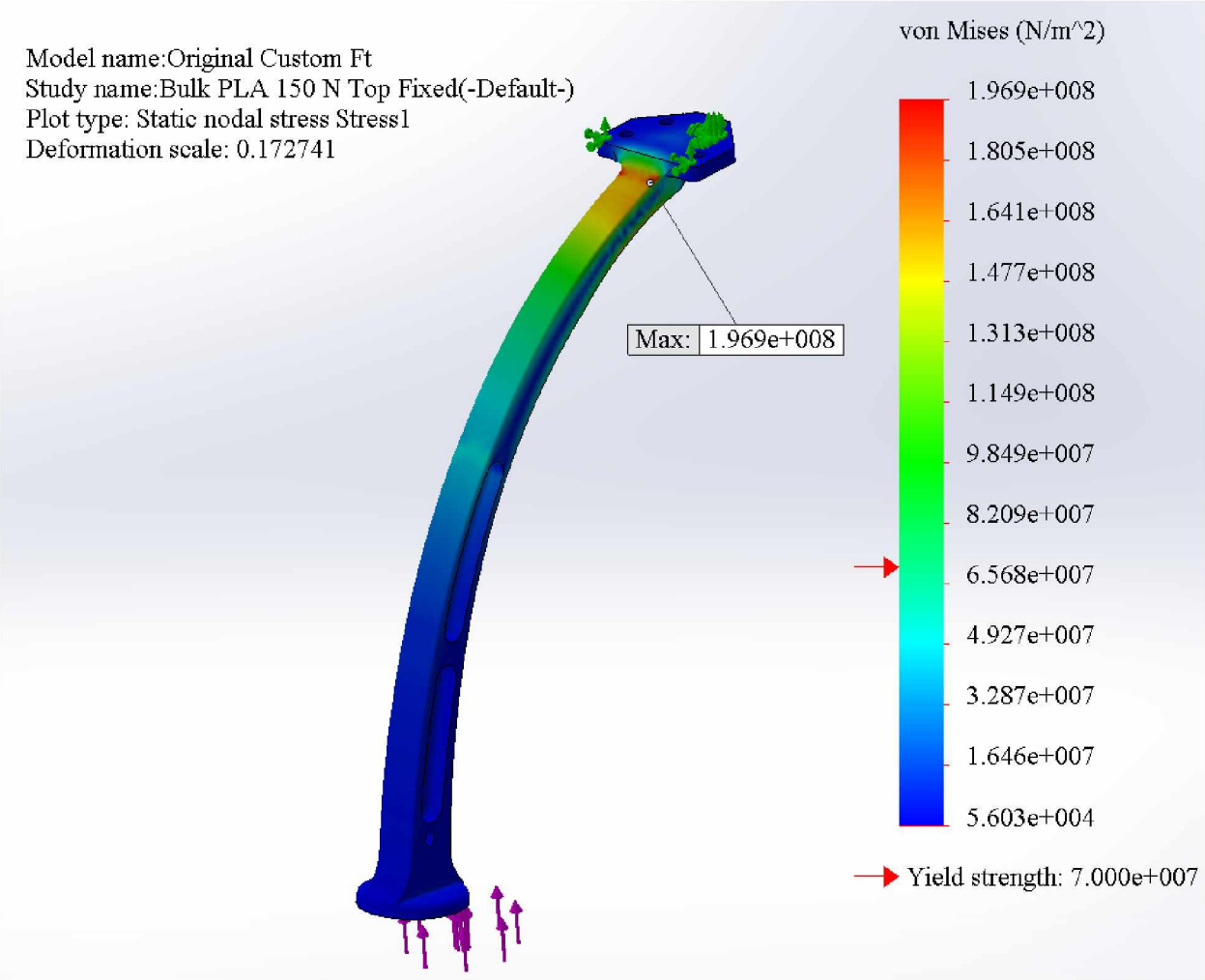

Figure 3.5: Original landing gear stress analysis with 150 N of force applied to the bottom with the top fixed and material of Bulk PLA

It can be noted that the fracture shown in Figure 3.4(a) is approximately in the same location as the maximum stress in Figure 3.5. Fixing the bottom and applying the stress on the top grants a different perspective which is shown in Figure 3.6. Similarly to the comparison between

the analysis in Figure 3.4 and the actual fracture in Figure 3.4(a), it can also be noted that Figure 3.5 shares the approximate location of fracture as Figure 3.4(b). Because the material for the stress analyses in Figures 3.5 and 3.6 was Bulk PLA, the part will consistently fracture under the force of 150 N.

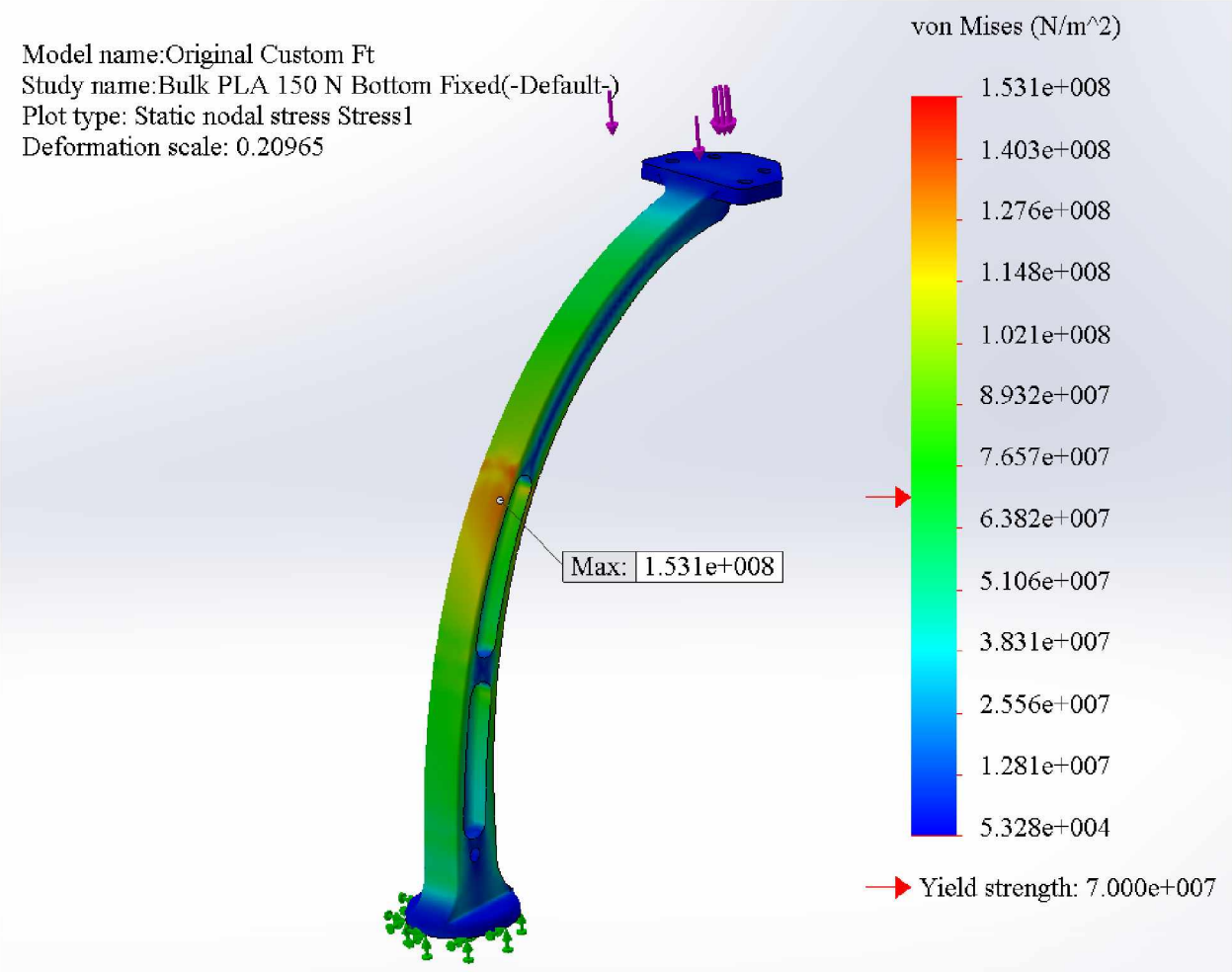

Figure 3.6: Original landing gear stress analysis with 150 N of force applied to the top with the bottom fixed and material of Bulk PLA

The landing gear was redesigned due to this failure and due to the need for a larger through hole for the pin. To analyze and compare with the previous design, the material properties of PLA using the porosity equations were calculated for both the original and final designs. These values are shown in Table 3.2 below.

Table 3.2: Porosity PLA Material Properties Calculation for Original and Final Custom Feet

	Original Custom Foot	Final Custom Foot
Surface Area, mm^2	9875.28	10489.30
Volume, mm^3	14265.09	26722.84
Calculated Porosity	0.200025	0.3948607
Young's Modulus, MPa	1891.74	940.15
UTS, MPa	14.74	3.10

The stress analysis of the redesigned foot using the material properties calculated with the porosity equations and a force of 16 N can be seen below in Figure 3.7. The yield stress is exceeded in the Porosity PLA stress analysis but not in 3D Printed PLA which indicates that it is unlikely but possible for the component to at least experience plastic deformation under the 16 N weight. The stress analysis illustrates that the force is more evenly distributed in the new design as there is no focus of stress like those found in Figures 3.5 and 3.6.

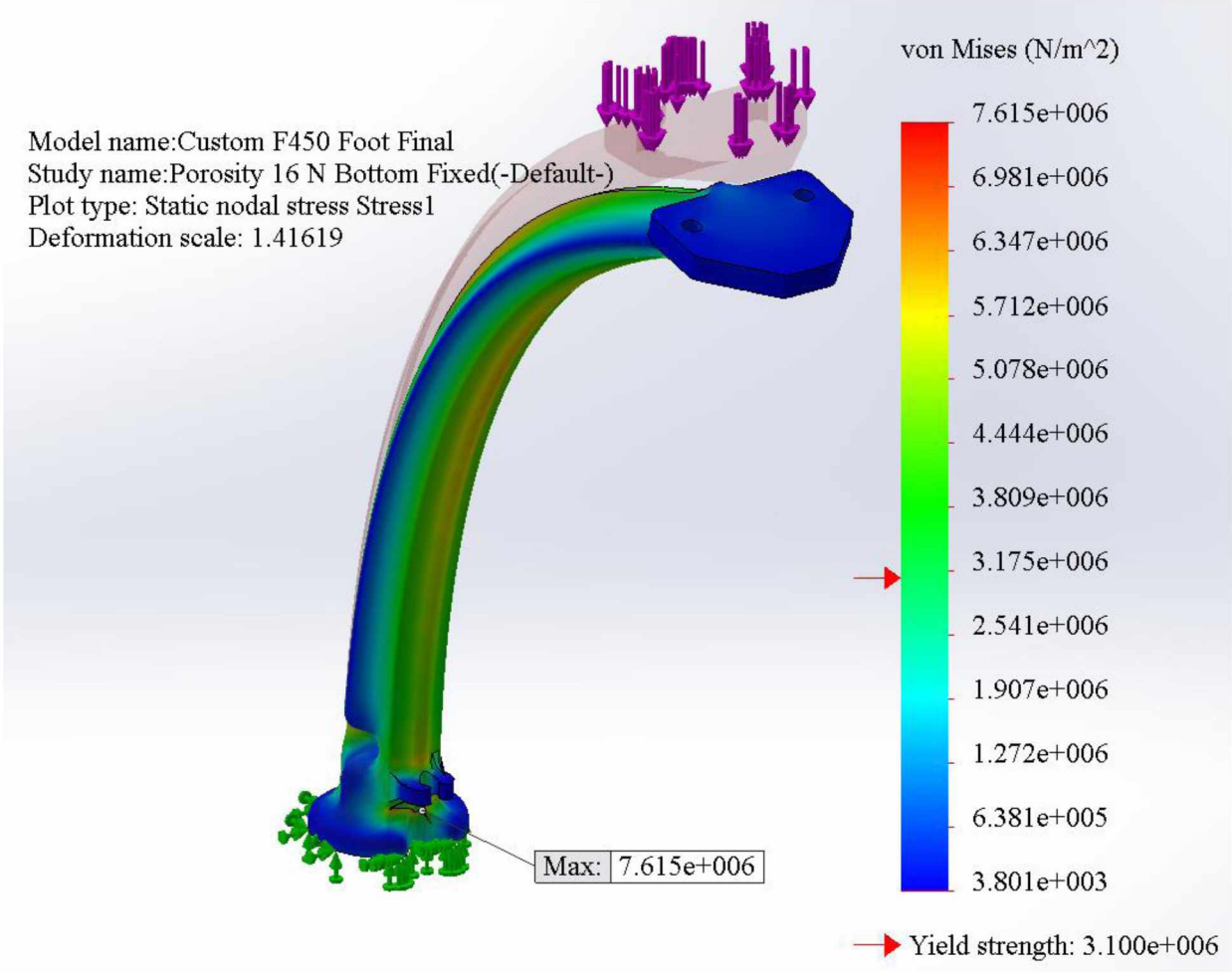

Figure 3.7: Final landing gear stress analysis with 16 N of force applied to the top with the bottom fixed and material of Porosity PLA

For a better comparison between the old and new legs, Figure 3.8 shows the stress analysis of the final landing gear under a 150 N force pushed from the bottom and the top fixed with a material of Bulk PLA. This shows that while the bottom fixed scenario results in more evenly distributed stress, the top fixed scenario still contains a high stress concentration at the top of the leg. Increasing the diameter at that location in a future design or redesigning the leg to allow for more impact absorption could mitigate this stress.

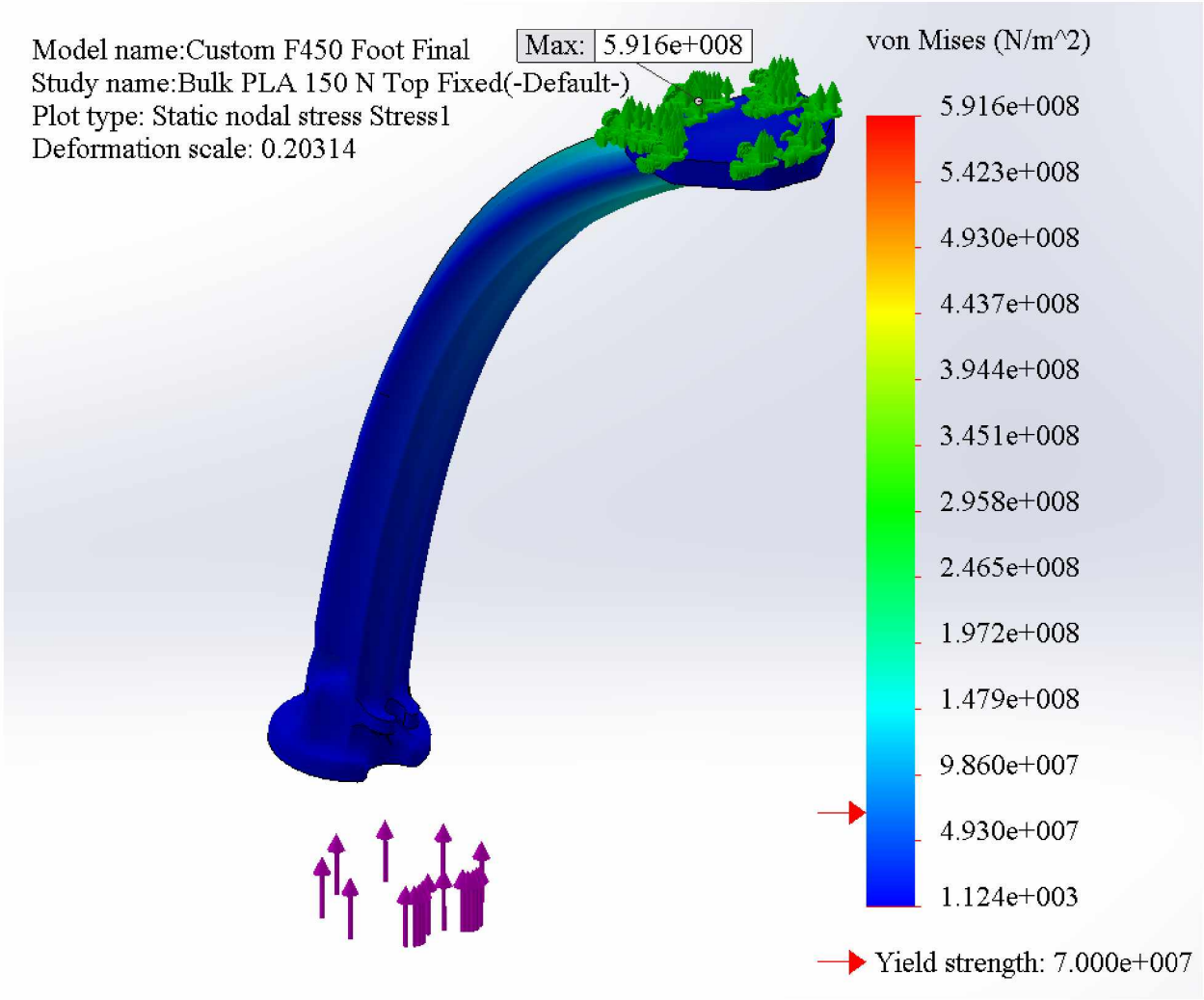

Figure 3.8: Final landing gear stress analysis with 150 N of force applied to the bottom with the top fixed and material of Bulk PLA

For a more direct comparison between the old design and the new, Table 3.3 below shows the maximum stress values in units of MPa obtained in the analyses for both 16 N and 150 N and both bottom and top fixed perspectives. The cells that are gray filled represent values that exceed the yield stress.

Table 3.3: Landing Gear Maximum Stress Comparison in Units of MPa

	Original Custom Foot		Final Custom Foot	
Material	Bottom Fixed	Top Fixed	Bottom Fixed	Top Fixed
16 N				
Bulk	16.33	21.01	7.615	35.14
3D Printed	17.57	21.01	7.830	35.24
Porosity	16.33	21.01	7.615	38.48
150 N				
Bulk	153.1	196.9	71.39	591.6
3D Printed	479.4	32.87	90.06	607.6
Porosity	153.1	196.9	71.39	311.7

From these data, it can be seen that while the new design experiences less stress in a bottom fixed scenario, it experiences much more in a top fixed scenario. It would appear that the original design experiences less stress than the new design. However, there is an additional change to the new design for which is not accounted in the values shown: the through hole was increased substantially to allow for the clearance of a pin. This increase was necessary and would not function in the original custom foot as it would introduce a major weak point. The higher stress values of the final design may also result from a less flexible part due to the great volume increase and less significant jump in surface area, as was seen in Table 3.2. A new design that allows for more flexibility to absorb the impact force may also result in less stress. This could also be accomplished simply by making the component out of a more flexible material.

3.3. Funneling Array

The passive guidance system serves two functions as mentioned previously: 1) relief on the automated landing tolerances and 2) point attached to the UGV suitable for connecting in some fashion to the UAV. A simple “pin-through” design was adopted for this project, and the funneling arrays accommodate this by allowing the pin to pass through it and the landing gear. Unlike the

landing gear, there were no fractures during tests and so no major redesigns were required; however, it was determined that a contact platform that could be easily removed from the bottom of the funnel would be beneficial for any construction or troubleshooting required. Thus, two designs for the funnel were used, one for the removable contact platform and one to house the electromagnets (EM). The material properties using the porosity equations for the funnel are shown below in Table 3.4.

Table 3.4: Porosity PLA Material Properties Calculation for Removable Platform and Electromagnet Funnel Designs

	Removable Platform	EM
Surface Area, mm^2	38536.93	46166.24
Volume, mm^3	49625.76	59779.51
Calculated Porosity	0.1452419	0.1480210
Young's Modulus, MPa	2255.72	2236.04
UTS, MPa	22.84	22.34

The stress analysis for the removable platform funnel design is shown below in Figure 3.9. This stress analysis was done using the porosity values and a force of 150 N applied downward to the pin-through holes with the vibration damping ball holes fixed. The fact that the maximum stress in this analysis does not exceed the UTS value from the porosity equation indicates that this component will probably not fracture under impact and thus does not need to be manufactured from a different material.

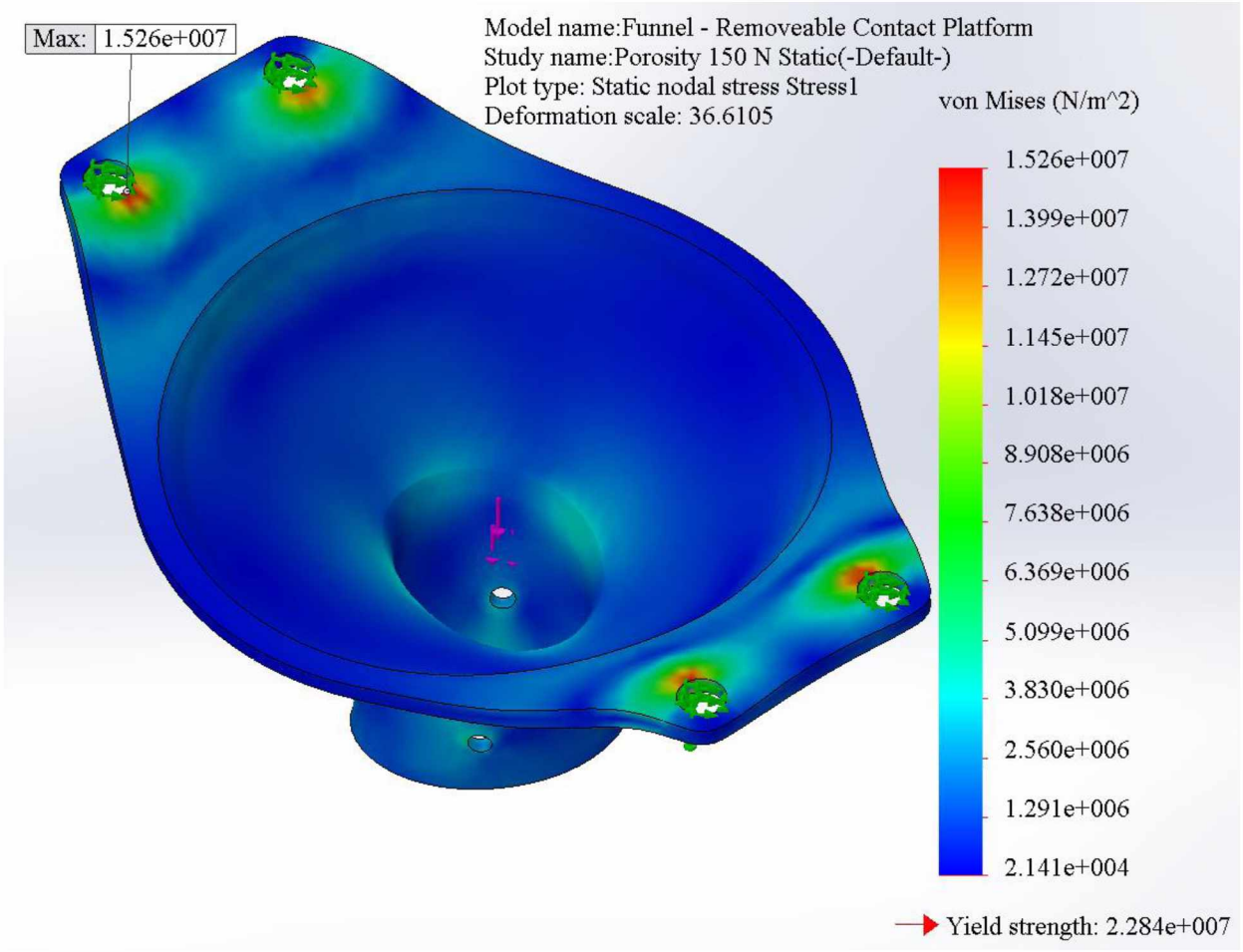

Figure 3.9: Removable contact platform funnel stress analysis with 150 N of force applied to the pin-through holes with the vibration damping ball holes fixed and material of Porosity PLA

Using the same values as Figure 3.9, the stress analysis for the electromagnet funnel design is shown below in Figure 3.10. It also does not exceed the UTS value, which is also used as the yield strength in these analyses due to the lack of information on calculating the yield strength based off of the porosity. Ergo, both funnel designs should withstand a force of 150 N without requiring a different material in production.

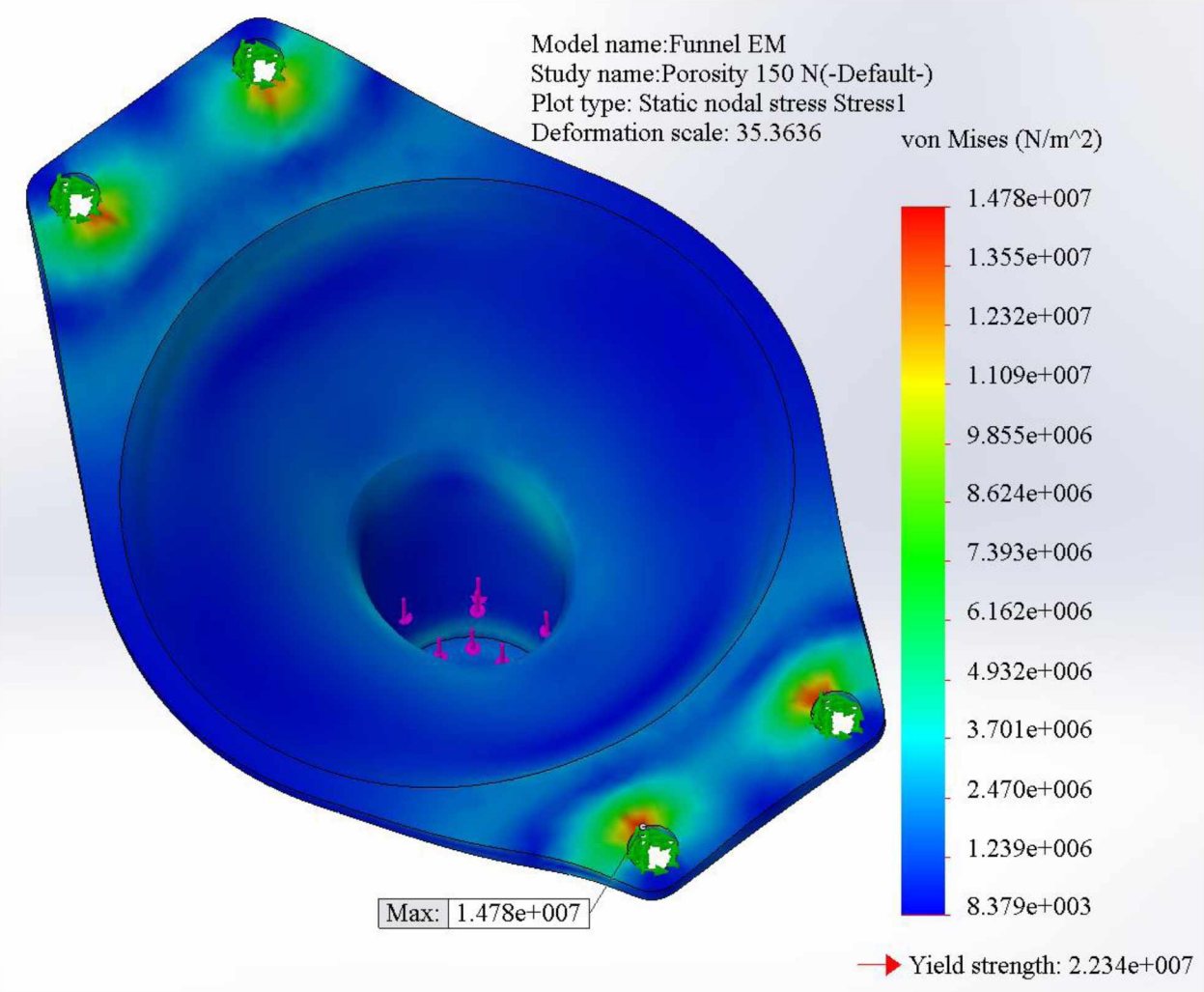

Figure 3.10: Electromagnet funnel stress analysis with 150 N of force applied to the pin-through holes with the vibration damping ball holes fixed and material of Porosity PLA

Two of the UAV's legs will land and rest on the contacts which are housed on the contact platform. Therefore, the contact platform should also be analyzed for its stress distribution. The contact platform's porosity calculations are shown in Table 3.5 below.

Table 3.5: Porosity PLA Material Properties Calculation for Contact Platform

Surface Area, mm^2	11140.19
Volume, mm^3	15589.26
Calculated Porosity	0.1855056
Young's Modulus, MPa	1983.41
UTS, MPa	16.55

The stress analysis for the removable contact platform is shown below in Figure 3.11. This stress analysis was done using the porosity values and a force of 150 N applied downward on the platform with the mounting screw holes fixed. Like the funnels, the fact that the maximum stress in this analysis does not exceed the UTS value from the porosity equation indicates that this component will probably not fracture under impact and thus does not need to be manufactured from a different material. This UTS value is relatively close to being reached in this analysis, however, and so the unknown yield strength may have been exceeded. To ensure this does not occur, the contact platform could be manufactured from a different material.

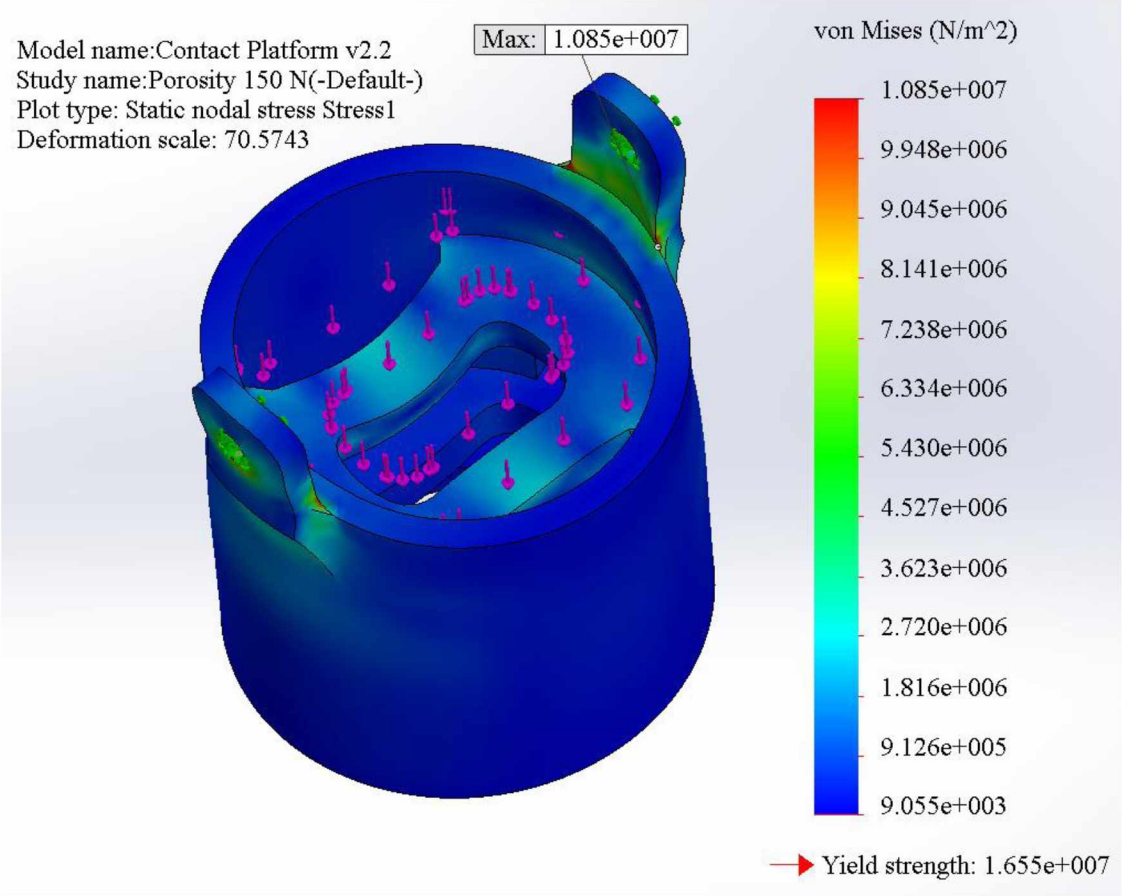

Figure 3.11: Contact platform stress analysis with 150 N of force applied to the platform with the mounting screw holes fixed and material of Porosity PLA

In order to mitigate the vibrations experienced by the UAV during transport, vibration damping balls are utilized between the funnels and the UGV. This requires a mount or adapter to connect UGV to damping ball to funnel. The material properties of PLA using the porosity equations were calculated for this funnel mount and are shown below in Table 3.6.

Table 3.6: Porosity PLA Material Properties Calculation for Funnel Mount

Surface Area, mm^2	5149.13
Volume, mm^3	6504.78
Calculated Porosity	0.135465
Young's Modulus, MPa	2326.08
UTS, MPa	24.70

Using these porosity values, the stress analysis shown in Figure 3.12 below was conducted using 150 N of applied to the main body with the mounting screw holes fixed. Although it is highly unlikely that this part would undergo the full impact force, as is true of any of these individual components, this analysis reveals that the porosity UTS will be exceeded if the funnel mount received the full impact of the UAV dropping from 0.15 m (about 6 inches); since the 3D printed PLA value was not exceeded, the component may or may not fail under such circumstances.

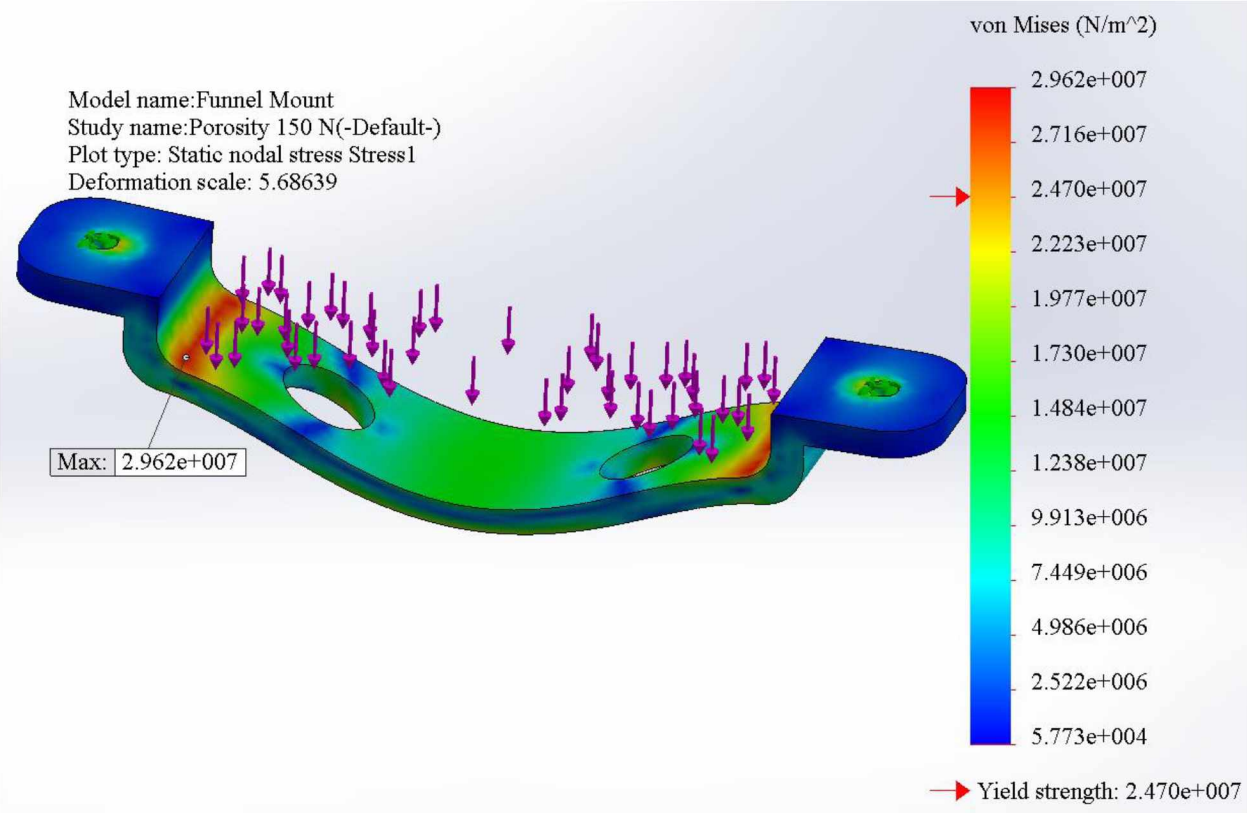

Figure 3.12: Funnel mount stress analysis with 150 N of force applied to the main body with the mounting screw holes fixed and material of Porosity PLA

3.4. Actuator

As mentioned in Chapter 2, a mechanism that latches and releases will require parts that move. This means an actuator of some sort must be present to receive and implement commands. An easy to obtain and command actuator is a servo or motor. This servo and the other pieces

composing the actuator need something that integrates them, and so a servo mount was designed. Figure 3.13 below shows the actuator assembly.

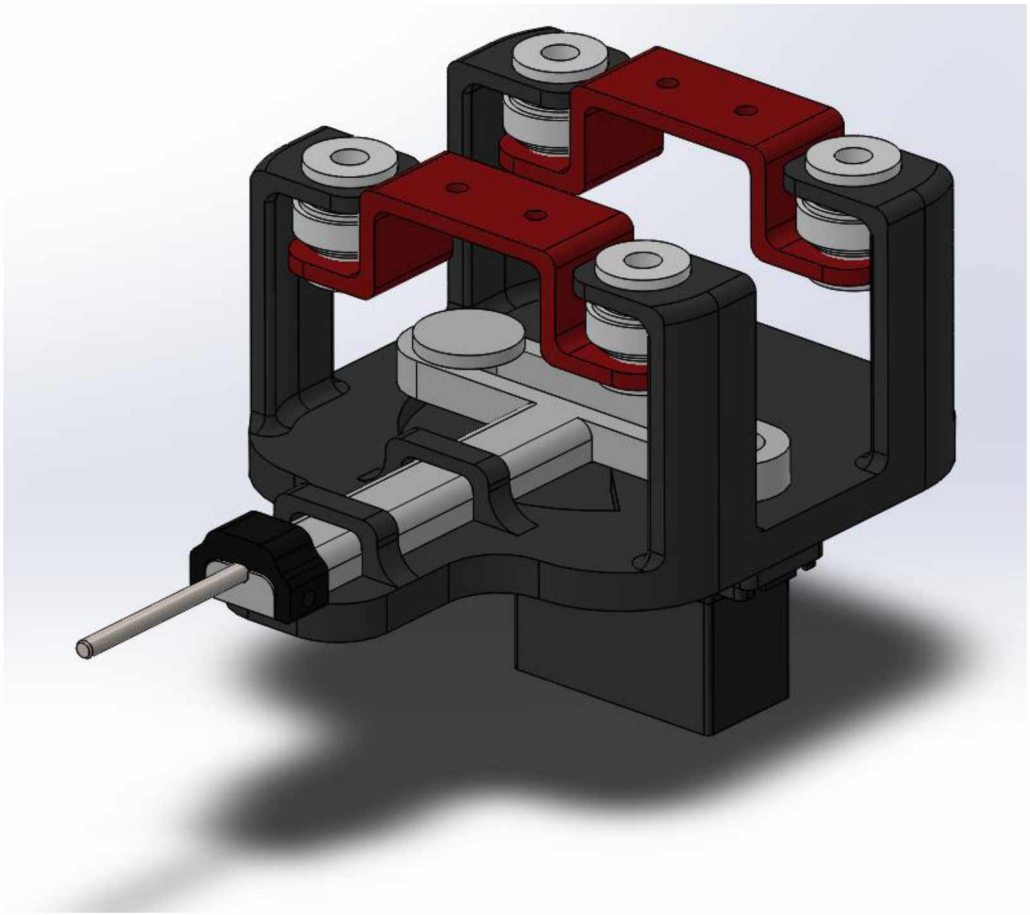

Figure 3.13: Actuator assembly comprised of a servo, servo mount, Scotch yoke, vibration damping balls, and adapter between damping balls and UGV

The material properties using the porosity equations for this servo mount is shown below in Table 3.7.

Table 3.7: Porosity PLA Material Properties Calculation for Servo Mount

Surface Area, mm^2	34405.85
Volume, mm^3	76375.25
Calculated Porosity	0.3571852138
Young's Modulus, MPa	1088.534288
UTS, MPa	4.191160778

The stress analysis for the servo mount using the porosity values and a concentrated force of 16 N applied downward on the end with the vibration damping ball holes fixed is shown below in Figure 3.14. The yield strength is exceeded in this analysis, and so the component may fail if it experienced the full weight of the UAV on the end. While this scenario is highly unlikely, it reveals that should the pin be extended through the funnel while the UAV attempts to land and the UAV drops from a sufficient height, the servo mount could break starting at the location of the maximum stress.

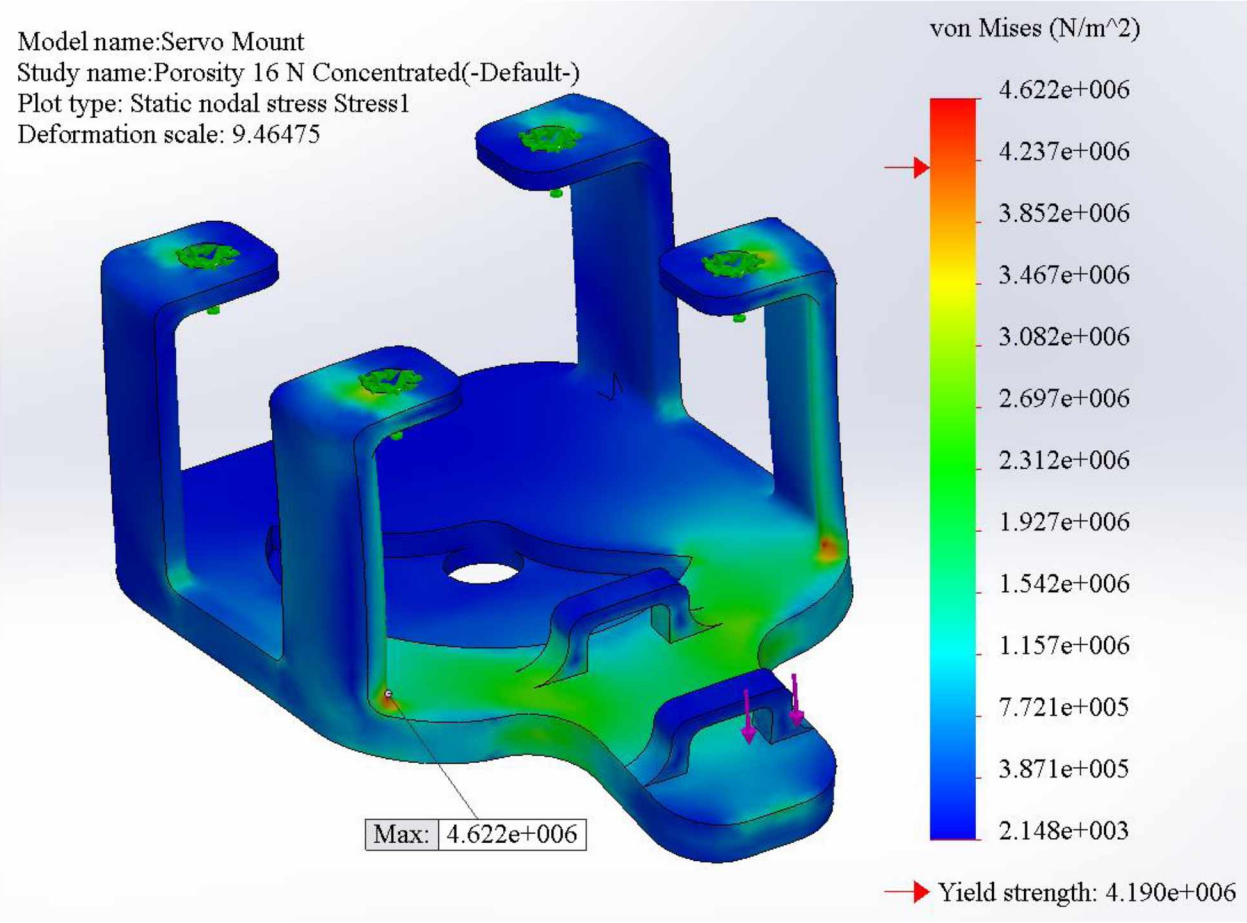

Figure 3.14: Servo mount stress analysis with 16 N of concentrated force applied to the end with the vibration damping ball holes fixed and material of Porosity PLA

This mount, like the funneling array, utilizes vibration damping balls to reduce the vibrations the UAV experiences through the pin in the landing gear while docked. Consequently, a mount or adapter for the servo mount is required, similar to the funnels. Table 3.8 below contains the porosity material properties.

Table 3.8: Porosity PLA Material Properties Calculation for Mount for the Servo Mount

Surface Area, mm^2	4691.24
Volume, mm^3	5839.40
Calculated Porosity	0.127805
Young's Modulus, MPa	2382.41
UTS, MPa	26.26

The stress analysis for the servo mount's mount using 150 N of force applied to the vibration damping ball holes with the screw holes fixed and material of Bulk PLA is shown below in Figure 3.15. The maximum stress exceeds the yield strength and UTS of the bulk PLA values, signifying that it would most likely fracture should it receive the full impact force of the UAV dropping. While this is unlikely to occur, a different material could be selected or the part could be thickened to ensure it could withstand such a force.

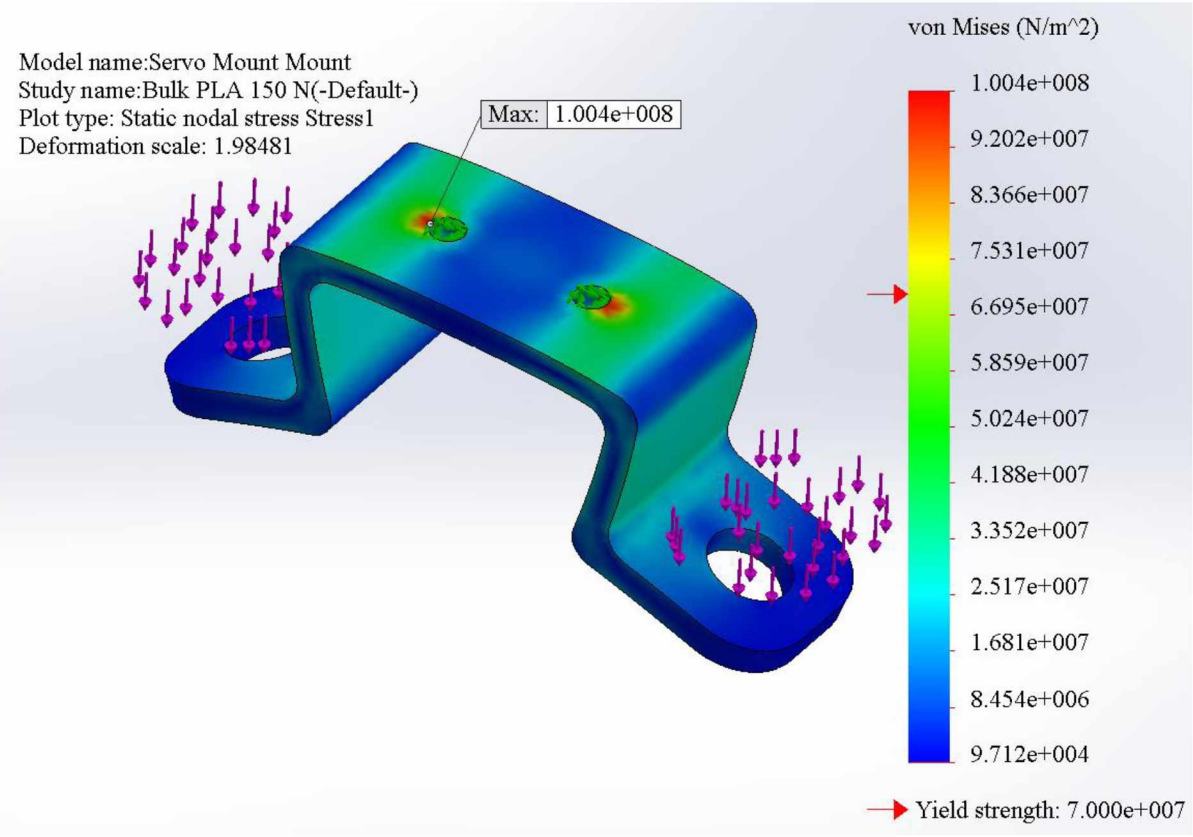

Figure 3.15: Servo mount mount stress analysis with 150 N of force applied to the vibration damping ball holes with the screw holes fixed and material of Bulk PLA

A Scotch yoke design was used to convert the rotational movement of the servo into linear movement. This necessitates an arm that is connected to the servo and a yoke that arm pushes. The arm will not encounter any significant forces due to the fact that the servo would give by rotating first, and so it does not need to be analyzed for stress. However, the Scotch yoke could experience force, though unlikely since the pins through the funnels would exert force on the funnels instead of the yoke. The porosity material properties for the Scotch yoke are shown below in Table 3.9.

Table 3.9: Porosity PLA Material Properties Calculation for Scotch Yoke

Surface Area, mm^2	6687.79
Volume, mm^3	11471.09
Calculated Porosity	0.2710418103
Young's Modulus, MPa	1488.628123
UTS, MPa	8.348859632

The stress analysis for the Scotch yoke is shown below in Figure 3.16 with porous PLA as the material. This was done using 16 N of force on the pin end with the portion of the bottom plane that would lie flat on the servo mount fixed. This analysis shows that the Scotch yoke would possibly fracture under these conditions. However, as with various other components, it is unlikely that the Scotch yoke would experience this much force directly, even under impact. The vibration damping balls would aid in absorbing the energy in the event of an impact such that the servo mount and Scotch yoke would receive a smaller, more distributed force.

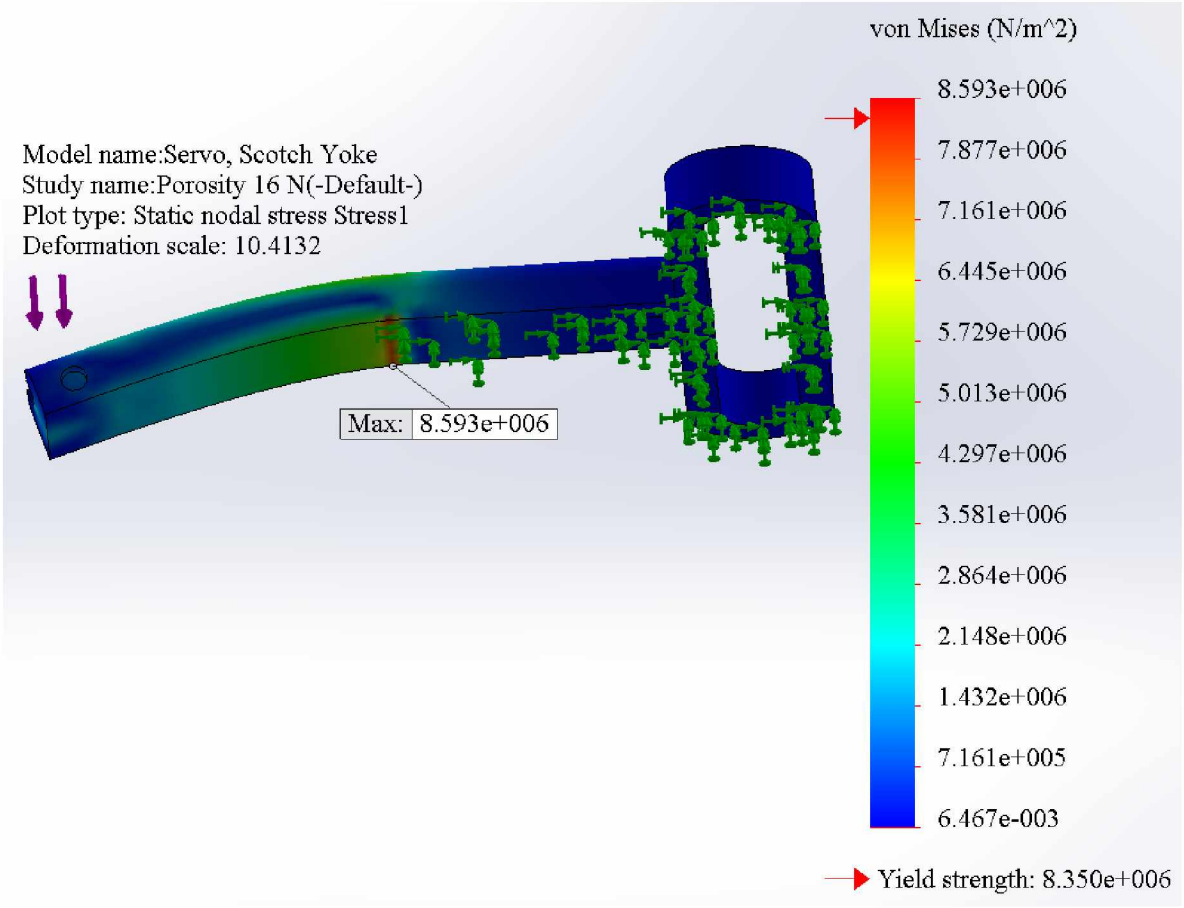

Figure 3.16: Scotch yoke stress analysis with 16 N of force applied to the pin end with the bottom plane in contact with the servo mount fixed and material of Porosity PLA

3.5. Pin

In this design for a locking mechanism, a pin is guided through one hole of a funnel, a hole in a landing gear, and through another hole on the other end of the funnel. This pin must be small enough so that the landing gear does not need to be of a infeasible size to accommodate the hole. The pin must also be strong enough to hold the UAV in place during transit in a bumpy, possibly inclined environment. Thus, two common but strong materials were evaluated for strength: aluminum and steel. Table 3.10 below shows the values for 6061 aluminum and chrome stainless steel from materials in SolidWorks' database.

Table 3.10: Material Properties of 6061 Aluminum and Chrome Stainless Steel from SolidWorks Database

	6061 Al	Chrome Stainless Steel
Property	Value	Value
Elastic Modulus, MPa	69000	200000
Poisson's Ratio	0.33	0.28
Shear Modulus, MPa	26000	77000
Mass Density, kg/m^3	2700	7800
Tensile Strength, MPa	124.08	413.61
Yield Strength, MPa	55.15	172.34

While aluminum is much lighter than steel, the component is small and so the weight would not majorly contribute to the overall weight for the ground vehicle. Steel is much stronger and would therefore be better suited for this purpose. Nevertheless, both materials were analyzed for comparison. Figure 3.17 below shows the stress analysis for 6061 aluminum with a 16 N force exerted on the circumference pointed in a single direction to replicate the scenario of the UAV's entire maximum takeoff weight exerted on the pin with the "head" fixed. The maximum stress in this analysis would exceed the UTS of 6061 aluminum, resulting in fracture in this scenario.

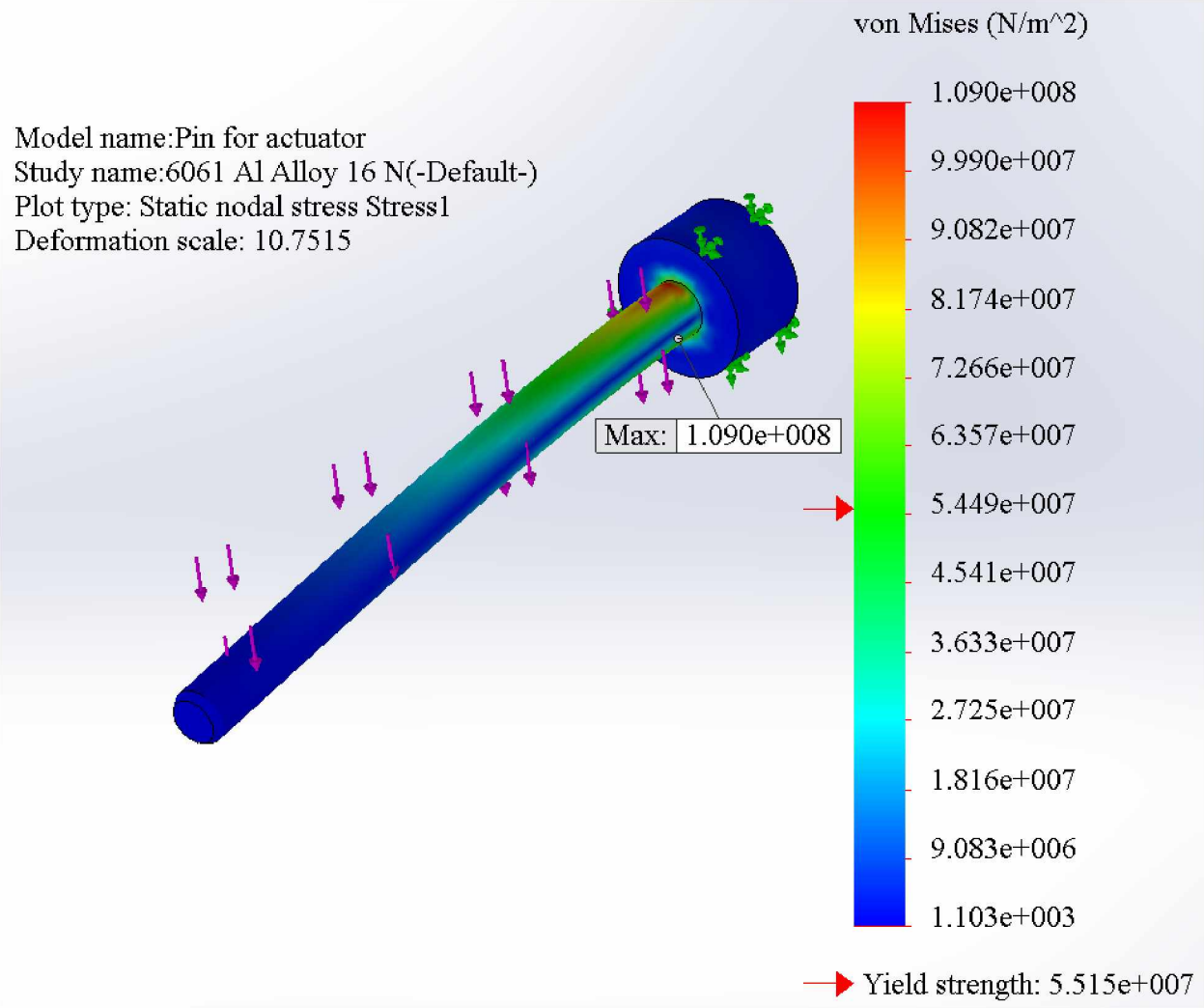

Figure 3.17: Pin stress analysis with 16 N force on circumference in a single direction with the head fixed and a material of 6061 Al

For a direct comparison, the same scenario is shown in Figure 3.18 but with the chrome stainless steel used as the material. This analysis shows that the stress would not exceed the yield strength, although it does approach it. Steel would hence be a better material for the pin.

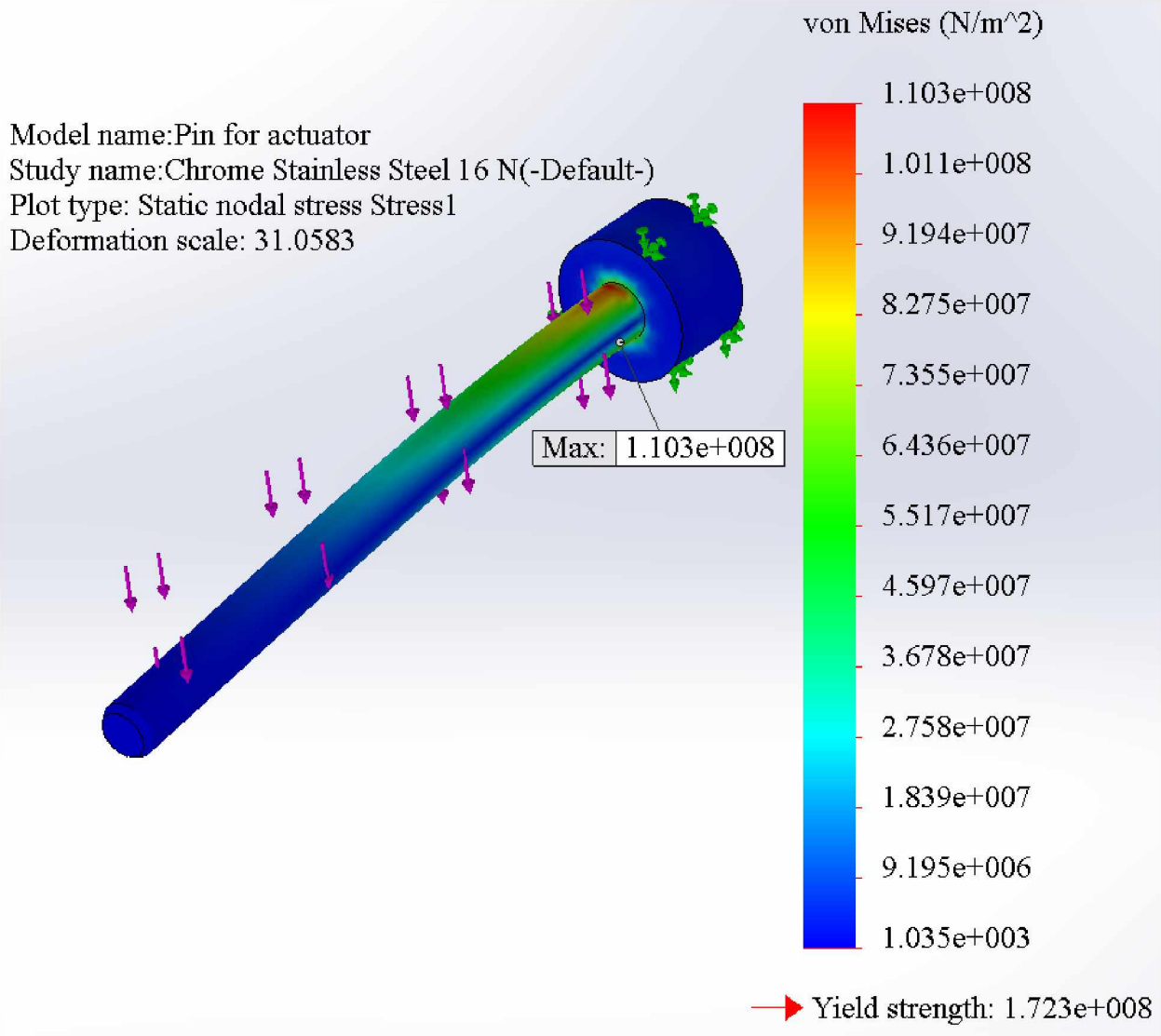

Figure 3.18: Pin stress analysis with 16 N force on circumference in a single direction with the head fixed and a material of Chrome Stainless Steel

In the event of an impact between the pin and the UAV should the pin be extended through the funnel, it is important to examine whether or not the pin would endure the hard landing. Figure 3.19 below shows the stress analysis assuming the pin alone receives the full impact with the head fixed as before. This analysis shows that it would fracture under the impact; like the previous setups for analyzing components, the pin would likely not receive the full impact force as it would react by transferring the force to the funnel and through the funnel to the vibration damping balls and funnel mount. The extreme is represented in this analysis, as with the previous, to determine the location and likelihood of failure.

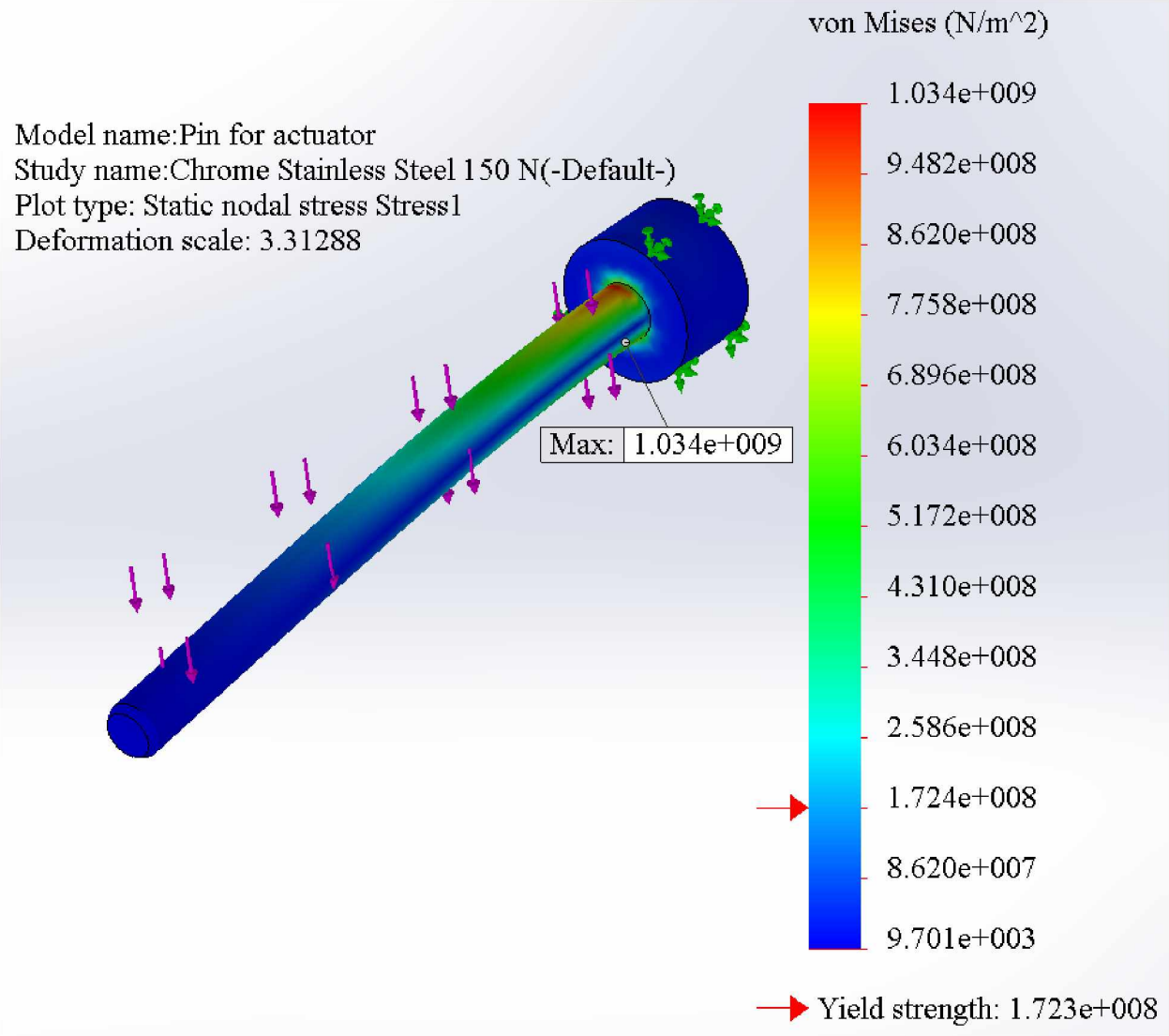

Figure 3.19: Pin stress analysis with 150 N force on circumference in a single direction with the head fixed and a material of Chrome Stainless Steel

3.6. Assembly

Once the components were all printed, they were all assembled. The contact boards with the pogo pins required feeding the wires through the contact platforms and soldering the wires to the board before setting the board inside the platforms. The contact platforms were then screwed onto the bottom of their two funnels, which had a hex nut adhered within the circumference. Figure 3.20 below shows the funnel assembly with the removable contact platform. The other set of funnels simply had electromagnets that sit in the bottom.

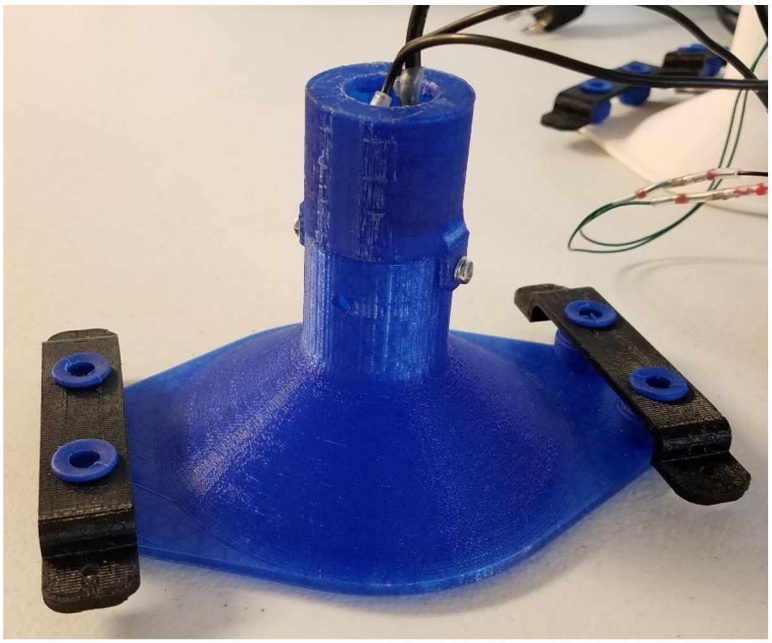

Figure 3.20: Funnel assembled with mount, vibration damping balls, and removable contact platform with contact board integrated

The funnels were screwed onto the landing pad, and the actuator assembly was carefully aligned to ensure the pin could go through the funnel. This configuration is shown below in Figure 3.21.

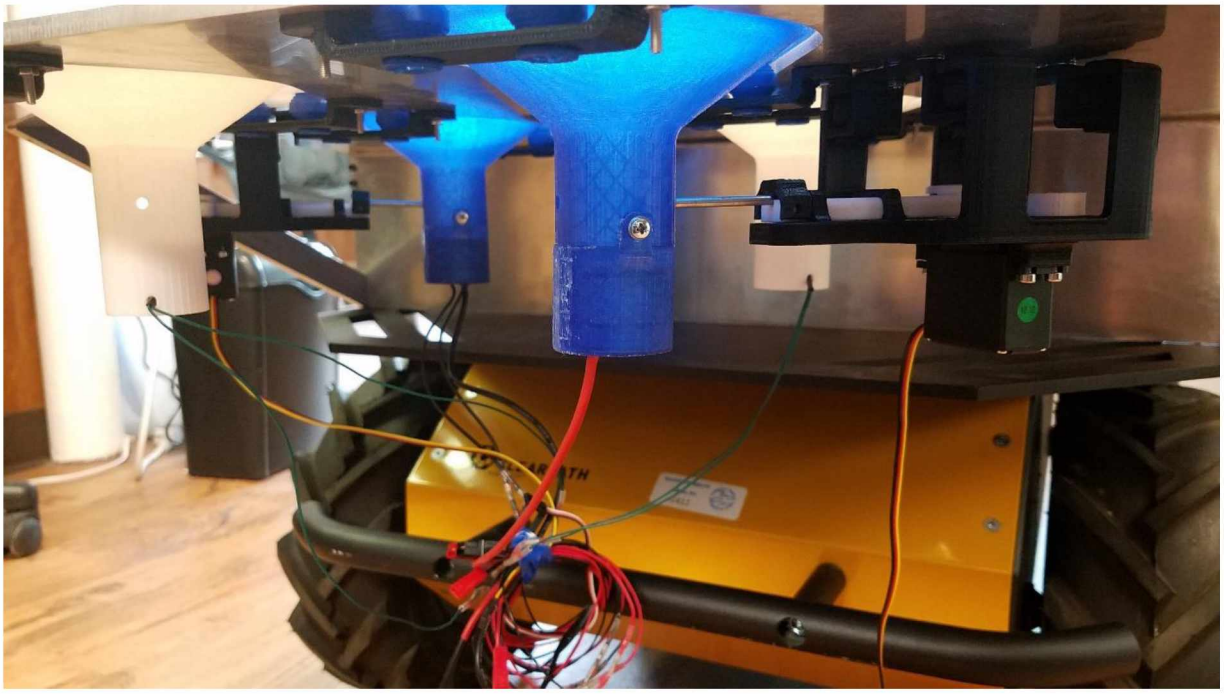

Figure 3.21: Components assembled onto landing plate extension

The electronics for the servo, electromagnets, and recharging capabilities are currently a temporary solution utilizing a breadboard and some various other boards that were available. These were mounted into a wooden frame that can be attached to the UGV. This mount is shown below in Figure 3.22 and was constructed by Sam Jefferies based upon design specifications provided by the author.

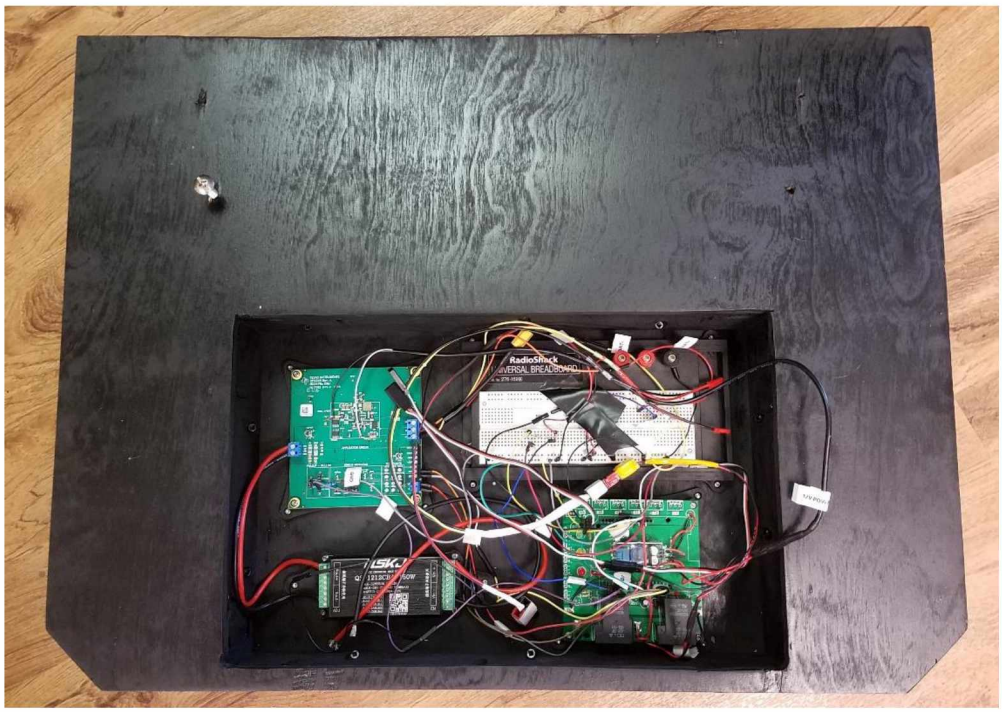

Figure 3.22: Electronics mount

The setup was tested on a wooden platform prior to integration with the UGV. Figure 3.23 below shows the successful pass of the pin through the funnel. The servo is activated once the pogo pins are depressed by the contact board that is adhered to the underside of the landing gear's foot. When a wire is soldered onto a similar board on the other foot and fed up to the UAV's battery, this system will also offer recharging capabilities.

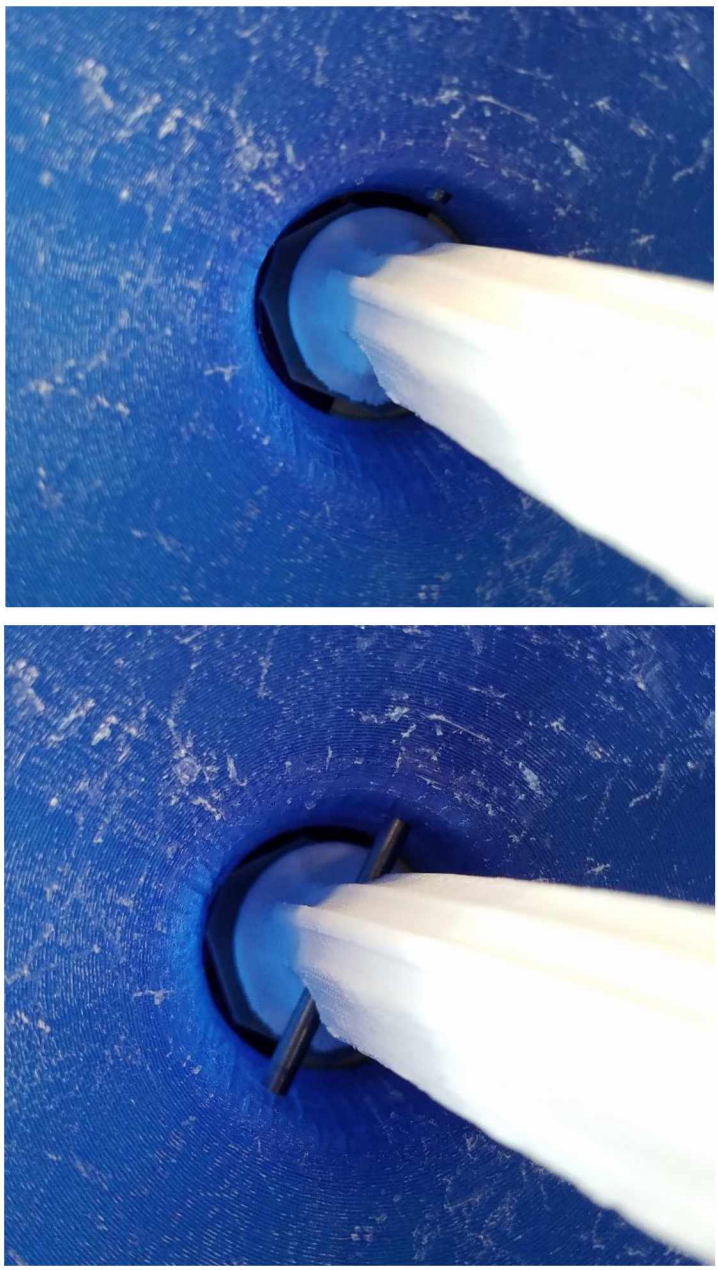

Figure 3.23: Successful test of the servo activating to push the pin through the leg and funnel

The total assembly is shown below in Figure 3.24.

Figure 3.24: Total assembly of latching mechanism

Chapter 4. Conclusions and Future Work

4.1. Conclusions

The components comprising the latching mechanism system were analyzed for stress using three different materials: Bulk PLA, 3D Printed PLA, and calculated Porosity PLA. For every component, two sets of forces were used, both 16 N and 150 N, one representing the maximum takeoff weight rounded up and the other an impact force of the UAV from 0.15 m (a little under 6 inches). In many instances, this was considered maximum and unlikely to be inflicted in such a manner to an individual component. Any part that would withstand the harshness of such a scenario would be sturdy enough to place appreciable confidence in it; any stress analysis that revealed a part to fail in such circumstances would provide a helpful qualitative mapping of locations of potential fracture points.

Though maximum theoretical conditions were utilized to analyze the stress of the components of the locking mechanism assembly, a few components were shown to succeed in not fracturing and so would be useful, such as the funnels. A few more components were shown to fail in the extreme scenarios but would be suitable for their designed use, such as the servo mounts. The most vital component is the landing gear leg, which was shown to be in doubt as to whether or not it could withstand any significant impact. This potentially warrants testing and redesign. The design could be used if the material was changed to a stronger, more flexible plastic. The probability of the UAV undergoing a hard or crash landing is dependent on the guidance and automated landing systems that are still in development, but the landing gear should be able to survive a reasonable drop distance. Some ruggedness is desirable, as well.

The parts that were shown to not exceed the yield strength under the 150 N load with Porosity PLA as the material were both funnel types and the contact platform. The funnel mount only exceeded the yield strength in the Porosity PLA analysis and so would also likely not fail under the more extreme condition. Additionally, the parts that did not exceed the yield strength under the 16 N load with Porosity PLA as the material were the Scotch yoke, mount for the servo mount, and the funnel mount. The servo mount exceeded only the Porosity PLA analysis and assumed a concentrated force. The landing gear exceeded all but the Bulk PLA yield strength when fixing the top portion and applying the force on the foot. When the foot was fixed and the force

applied to the top, the stress exceeded only the Porosity PLA yield strength. This implies that given the right force and angle at which the UAV lands, the landing gear may fracture. However, the landing gear was not designed such that the UAV lands on a single leg but rather four to distribute the weight.

4.2. Future Development

This project fully developed one possible latching mechanism, but there are other methods of securing the UAV to the UGV that may prove more reliable and less likely to fail. These methods should be investigated. Figure 4.1 below illustrates one potential design concept, showing a new footprint for the landing gear (on the left) and a receptacle that can be rotated to lock the landing gear in place (on the right). With this design, a different system for sensing the UAV's docking and recharging the UAV's battery may be required since the rotation of the latch may scrape the contact board against the pogo pins excessively resulting in too much wear.

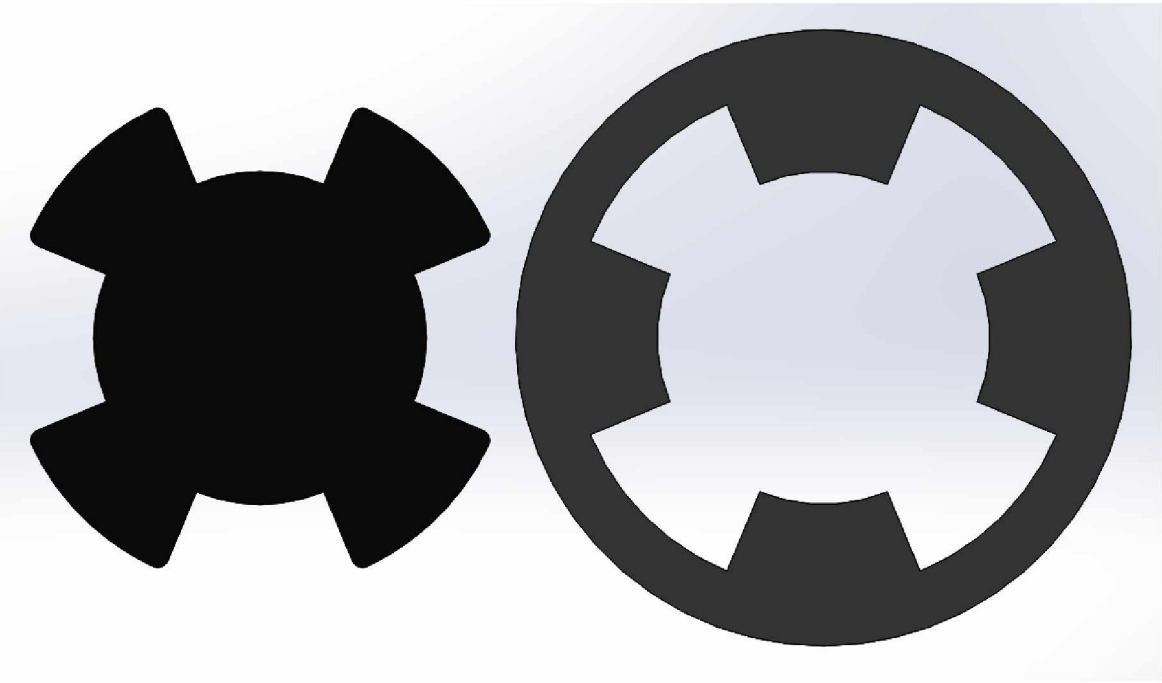

Figure 4.1: Concept for an alternative latching mechanism design with a different footprint for the landing gear (left) and a rotating receptacle (right)

The landing gear itself could be redesigned or improved to ensure it does not fracture in the event of a hard landing, as the stress analysis revealed the likelihood of rupture after a 0.15 m

(about 6 inches) drop. The "neck" or upper portion of the leg is a weak point as is shown in the stress analysis, and so this location could be bolstered. Allowance in the design for some give during an impact could also reduce the impact force felt by the legs and thus reduce the stress. This could also be accomplished using a stronger, more flexible material.

Due to the weight of the UAV's payload, a more powerful aircraft will likely be required, such as the hexacopter F550, pictured below in Figure 4.2. If this is the case, a similar landing platform would need to be constructed as the F550 has a different footprint than the F450, and the funneling array would thus need to be adjusted to accommodate that disparity. The landing gear may also need to be redesigned if the F550 is selected for the final vehicle as the stress analyses show that a single landing gear leg possibly could not withstand the lesser maximum takeoff weight of the F450. With the weight distributed among four legs, it would likely hold the F550, but more mass means more impact force should it perform a hard landing.

Figure 4.2: F550 with mounted LiDAR

As for the overall project, there is ongoing work to complete the automated landing, LiDAR mapping, and communications systems. These aspects of the overall project are still in development.

References

[1] Mine Safety and Health Administration, 2017, "Mining Facts 2015," National Institute for Occupational Safety and Health Mining Program, from https://www.cdc.gov/niosh/mining/works/statistics/factsheets/miningfacts2015.html, Accessed July 25, 2017.

[2] Mine Safety and Health Administration, n.d., "The History of Mine Rescue," United States Department of Labor, from https://arlweb.msha.gov/TRAINING/LIBRARY/historyofminerescue/page11.asp, Accessed July 25, 2017.

[3] Shames, I.H., Pitarresi, J.M., 2000, Introduction to Solid Mechanics, Prentice Hall, New Jersey, pp. 1-2, Chap. 1.

[4] Beer, F.P., Johnston, E.R., DeWolf, J.T., Mazurek, D.F., 2009, Mechanics of Materials, McGraw Hill, New York, pp. 5, 49, 52-53, 56-57, 423-430, 451-453, Chap. 1, 2, 7.

[5] SolidWorks, n.d., "Linear Stress Analysis," from http://www.solidworks.com/sw/products/simulation/stress-analysis.htm, Accessed June 14, 2017.

[6] SolidWorks, n.d., "Nonlinear Analysis," from http://www.solidworks.com/sw/products/simulation/non-linear-analysis.htm, Accessed June 14, 2017.

[7] Boresi, A.P., Schmidt, R.J., 2003, Advanced Mechanics of Materials, John Wiley & Sons, Inc., pp. 42, 117-122 Chap. 2, 4.

[8] Keles, O., Blevins, C.W., Bowman, K.F., 2017, "Effect of Build Orientation on the Mechanical Reliability of 3D Printed ABS," Rapid Prototyping Journal, 23(2), pp. 320-328.

[9] Farsadi, A., Solati-Hashjin, M., Asadi-Eydivand, M., Abu Osman, N.A., 2014, "Effect of Layer Thickness and Printing Orientation on Mechanical Properties and Dimensional Accuracy of 3D Printed Porous Samples for Bone Tissue Engineering," PLoS ONE, 9(9).

[10] Lee, C.S., Kim, S.G., Kim, H.J., Ahn, S.H., 2007, "Measurement of Anisotropic Compressive Strength of Rapid Prototyping Parts," Journal of Materials Processing Technology, 187-188, pp. 627-630.

[11] Torrado, A.R., Roberson, D.A., 2016, "Failure Analysis and Anisotropy Evaluation of 3D-Printed Tensile Test Specimens of Different Geometries and Print Raster Patterns," Journal of Failure Analysis and Prevention, 16(1), pp. 154-164.

[12] Merklein, M., Plettke, R., Junker, D., Schaub, A., Ahuja, B., 2015, "Mechanical Testing of Additive Manufactured Metal Parts," Key Engineering Materials, 651-653, pp. 713-718.

[13] Lanzotti, A., Grasso, M., Staiano, G., Martorelli, M., 2015, "The Impact of Process Parameters on Mechanical Properties of Parts Fabricated in PLA with an Open-Source 3-D Printer," Rapid Prototyping Journal, 21(5), pp. 604-617.

[14] Sood, A.K., Ohdar, R.K., Mahapatra, S.S., 2010, "Parametric Appraisal of Mechanical Property of Fused Deposition Modelling Processed Parts," Materials & Design, 31(1), pp. 287-295.

[15] Tymrak, B.M., Kreiger, M., Pearce, J.M., 2014, "Mechanical Properties of Components Fabricated with Open-Source 3-D Printers Under Realistic Environmental Conditions," Materials & Design, 58(1), pp. 242-246.

[16] Torres, J., Cotelo, J., Karl, J., Gordon, A.P., 2015, "Mechanical Property Optimization of FDM PLA in Shear with Multiple Objective," JOM, 67(5), pp. 1183-1193.

[17] Alvarez, K.L., Lagos, R.F., Aizpun, M., 2016, "Investigating the Influence of Infill Percentage on the Mechanical Properties of Fused Deposition Modelled ABS Parts," Ingenieria e Investigacion, 36(3), pp. 110-116.

[18] Gao, H., Kaweesa, D.V., Moore, J., Meisel, N.A., 2017, "Investigating the Impact of Acetone Vapor Smoothing on the Strength and Elongation of Printed ABS Parts," JOM, 69(3), pp. 580-585.

[19] Choren, J.A., Heinrich, S.M., Silver-Thorn, M.B., 2013, "Young's Modulus and Volume Porosity Relationships for Additive Manufacturing Applications," Journal of Materials Science, 48(15), pp. 5103-5112.

[20] Knudsen, F.P., 1959, "Dependence of Mechanical Strength of Brittle Polycrystalline Specimens on Porosity and Grain Size," Journal of the American Ceramic Society, 42(8), pp. 376-387.

[21] Rudakevych, P., Clark, S., Wallace, J., 2007, "Integration of the Fido Explosives Detector onto the PackBot EOD UGV," Proc. SPIE, Unmanned Systems Technology IX, 6561.

[22] Kaneko, K., Ito, K., Iwahori, K., Anbe, Y., 2015, "Development of Mobile Sensor for Volcanic Observation "HOMURA"; Test Campaign at Kirishima Iwo-yama, SW Japan," American Geophysical Union Fall Meeting, Abstract PA43C-2199.

[23] MacArthur, E.Z., MacArthur, D., Crane, C., 2005, "Use of Cooperative Unmanned Air and Ground Vehicles for Detection and Disposal of Simulated Mines," Proc. SPIE, Intelligent Systems in Design and Manufacturing VI, 5999.

[24] Subhan, M.A., Bhide, A.S., 2015, "Unmanned Ground Vehicle (UGV's) for Coal Mines," International Journal of Innovative Research in Advanced Engineering, 1(2), pp. 152-159.

[25] Li, J., Deng, G., Luo, C., Lin, Q., Yan, Q., Ming, Z., 2016, "A Hybrid Path Planning Method in Unmanned Air/Ground Vehicle (UAV/UGV) Cooperative Systems," IEEE Transactions on Vehicular Technology, 65(12), pp. 9585-9596.

[26] Minaeian, S., Liu, J., Son, Y.J., 2016, "Vision-Based Target Detection and Localization via a Team of Cooperative UAV and UGVs," IEEE Transactions on Systems, Man, and Cybernetics: Systems, 46(7), pp. 1005-1016.

[27] Dhiman, N.K., Deodhare, D., Khemani, D., 2015, "Where am I? Creating Spatial Awareness in Unmanned Ground Robots Using SLAM: A Survey," Sadhana Academy Proceedings in Engineering Sciences, Indian Academy of Sciences, 40(5), pp. 1385-1433.

[28] Munguia, R., Urzua, S., Grau, A., 2016, "Delayed Monocular SLAM Approach Applied to Unmanned Aerial Vehicles," PLoS One, 11(12).

[29] Hervas, J.R., Reyhanoglu, M., Tang, H., 2014, "Nonlinear Automatic Landing Control of Unmanned Aerial Vehicles on Moving Platforms via a 3D Laser Radar," 10th International Conference on Mathematical Problems in Engineering, Aerospace and Sciences, AIP Conf. Proc. 1637, pp. 907-917.

[30] Zhang, X., Liu, P., Zhang, C., 2015, "An Integration Method of Inertial Navigation System and Three-Beam Lidar for the Precision Landing," Mathematical Problems in Engineering, 2016.

[31] Kendoul, F., Ahmed, B., 2012, "Bio-Inspired TauPilot for Automated Aerial 4D Docking and Landing of Unmanned Aircraft Systems," 2012 IEE/RSJ International Conference on Intelligent Robots and Systems, IEEE, pp. 480-487.

[32] Yang, T., Li, G., Li, J., Zhang, Y., Zhang, X., Zhang, Z., Li, Z., 2016, "A Ground-Based Near Infrared Camera Array System for UAV Auto-Landing in GPS-Denied Environment," Sensors, 16(9).

[33] Mahoor, M.H., Godzdanker, R., Dalamagkidis, K., Valavanis, K.P., 2011, "Vision-Based Landing of Light Weight Unmanned Helicopters on a Smart Landing Platform," Journal of Intelligent & Robotic Systems, 61(1-4) pp. 251-265.

[34] Leonard, J., Aldhaher, S., Savvaris, A., Tsourdos, A., 2012, "Automated Recharging Station for Swarm of Unmanned Aerial Vehicles," Proceedings of the ASME 2012 International Mechanical Engineering Congress & Exposition, ASME, pp. 607-614.

[35] Michini, B., Toksoz, T., Redding, J., Michini, M., How, J., Vavrina, M., Vian, J., 2011, "Automated Battery Swap and Recharge to Enable Persistent UAV Missions," American Institute of Aeronautics and Astronautics.

[36] Swieringa, K.A., Hanson, C.B., Richardson, J.R., White, J.D., Hasan, Z., Qian, E., Girard, A., 2010, "Autonomous Battery Swapping System for Small-Scale Helicopters," 2010 IEEE International Conference on Robotics and Automation, IEEE, pp. 3335-3340.

[37] Palomeras, N., Ridao, P., Ribas, D., Vallicrosa, G., 2014, "Autonomous I-AUV Docking for Fixed-base Manipulation," Proceedings of the 19th World Congress, The International Federation of Automatic Control, pp. 12160-12165.

[38] Byun, Y., Song, J., Song, W., Kang, B., 2016, "Conceptual Study of a Smart Docking System for VTOL-UAV," Journal of Aerospace Engineering, 29(2).

[39] Mullens, K., Burmeister, A., Wills, M., Stroumtsos, N., Denewiler, T., Pachura, J., Prior, G., Hawkins, B., 2006, "Automated Launch, Landing and Refueling Technologies for Increased UGV-UAV Effectiveness," International Joint Topic: 9th Emergency Preparedness and Response/11th Robotics and Remote Systems for Hazardous Environments, pp. 164-170.

[40] Thomas, P.R., Bhandari, U., Bullock, S., Richardson, T.S., du Bois, J.L., 2014, "Advances in Air to Air Refuelling," Progress in Aerospace Sciences, 71, pp. 14-35.

[41] Flores-Abad, A., Ma, O., Pham, K., Ulrich, S., 2014, "A Review of Space Robotics Technologies for On-Orbit Servicing," Progress in Aerospace, 68, pp. 1-26.

[42] Medina, A., Tomassini, A., Suatoni, M., Aviles, M., Solway, N., Coxhill, I., Paraskevas, I.S., Rekleitis, G., Papadopoulos, E., Krenn, R., Brito, A., Sabbatinelli, B., Wollenhaupt, B., Vidal, C., Aziz, S., Visentin, G., 2017, "Towards a Standardized Grasping and Refuelling On-Orbit Servicing for Geo Spacecraft," Acta Astronautica, 134, pp. 1-10.

[43] Daly, J.M., Ma, Y., Waslander, S.L., 2011, "Coordinated Landing of a Quadrotor on a Skid-Steered Ground Vehicle in the Presence of Time Delays," 2011 IEEE/RSJ International Conference on Intelligent Robots and Systems, IEEE, pp. 4961-4966.

[44] Clearpath Robotics, n.d., "Husky Unmanned Ground Vehicle," from https://www.clearpathrobotics.com/husky-unmanned-ground-vehicle-robot, Accessed July 11, 2017.

[45] DJI, n.d., "Flame Wheel ARF Kit," from http://www.dji.com/flame-wheel-arf/spec, Accessed July 12, 2017.

[46] Weaver, J.N., Frank, D.Z., Schwartz, E.M., Arroyo, A.A., 2013, "UAV Performing Autonomous Landing on USV Utilizing the Robot Operating System," ASME District F - Early Career Technical Conference, ASME, pp. 119-124.

[47] The Engineering Toolbox, n.d., "Impact Force," from http://www.engineeringtoolbox.com/impact-force-d_1780.html, Accessed August 1, 2017.